Arabian Journal of Geosciences (2021) 14: 1138
https://doi.org/10.1007/s12517-021-07495-4

ORIGINAL PAPER

# Alteration patterns related to copper mineralization in dioritic rocks at the Dara area, north Eastern Desert, Egypt

Hossam A. Helba[1] · Mohamed A. Ghonaim[2] · Sobhy O. Khalil[1] · Ahmed M. El Makky[3]

Received: 2 January 2021 / Accepted: 31 May 2021 / Published online: 9 June 2021


## Abstract

The Dara copper mineralization is one of more than 15 copper occurrences distributed in the Neoproterozoic crust of the Eastern Desert of Egypt. The mineralization is hosted by calc-alkaline diorite and granodiorite rocks of I-type affinity and occurs as disseminated grains within NW trending veins and shear zones. Hydrothermal and supergene alteration signs were observed around the mineralized quartz veins. Major oxide and selected trace element analysis combined with textural relations and mineral associations was used to characterize and quantify the alteration processes in the Dara occurrence and to shed light on the nature of the invading hydrothermal fluids. Sericite-pyrite and chlorite-sericite alteration zones were recognized. Based on mass balance data, two successive hydrothermal stages were suggested. Initial fluids characterized by high $aH^+$ and $K^+$ activity are suggested for both stages. However, the first hydrothermal stage is characterized by fluids enriched in Cu content, whereas the second hydrothermal stage is characterized by fluids of higher $Fe^{2+}$ and $Mg^{2+}$ activities. Magmatic- rather than metamorphic-related fluids can be suggested based on the physicochemical conditions of formation of the hosted rocks and alteration products. Copper may be leached from the gabbro-diorite country rock that contains up to 0.9 wt.% Cu. The copper mineralization of the Dara area may belong to the magmatic-hydrothermal iron oxide-copper-gold (IOCG) deposit category rather than to the porphyry copper system.

**Keywords** Copper mineralization · Hydrothermal alteration · Mass balance · Mineral paragenesis · Dara area-Egypt

## Introduction

Porphyry and epithermal copper deposits constitute the main resources for Cu production in the world (Sillitoe 1998, 2010; Hedenquist et al. 2018). Iron oxide-copper-gold (IOCG) deposits of magmatic-hydrothermal origin, identified first by Hitzman et al. (1992), have many similarities to the porphyry Cu deposits (Barton and Johnson 2000; Groves et al. 2010). The former, however, are S-poor with abundant magnetite and/or hematite and more dominated in Precambrian rocks (Williams et al. 2005; Richards and Mumin 2013). Both form vein-type Cu mineralization and are commonly associated with alteration haloes. The composition, zonation, and extent of these haloes are structurally and lithologically controlled (Sillitoe 2010; Groves et al. 2010; Mumin et al. 2010; Cooke et al. 2014; Wilkinson et al. 2015; Neal et al. 2018).

The basement rocks exposed in the Eastern Desert and Sinai Peninsula of Egypt are known to host copper mineralization, with more than 15 occurrences so far identified (Fig. 1a). These occurrences have recently received great attention because of the controversy about their genesis and the need to evaluate their ore potentiality (Botros and Wetait 1997; Ahmed and Gharib 2016; Khalifa et al. 2016). Some of these occurrences were identified as porphyry copper-related deposits (Um Mungol, Hamash, and Um Garayat, # 6, 14, and 16, respectively - Fig. 1a) (Botros and Wetait 1997; Ivanov and Hussein 1972), while some others have been suggested as volcanogenic massive sulfide-related deposits (Um Samiuki occurrence, # 15 in Fig. 1a) (Hussein et al. 1977; Rasmy 1982), and others are still controversial.

Responsible Editor: Domenico M. Doronzo

✉ Hossam A. Helba
hhhelba@yahoo.com

[1] Geology Department, Faculty of Science, Alexandria University, Moharram B, Alexandria ey-21511, Egypt

[2] Egyptian Mineral Resources Authority (EMRA), Cairo, Egypt

[3] Biological and Geological Sciences Department, Faculty of Education, Alexandria University, Alexandria, Egypt

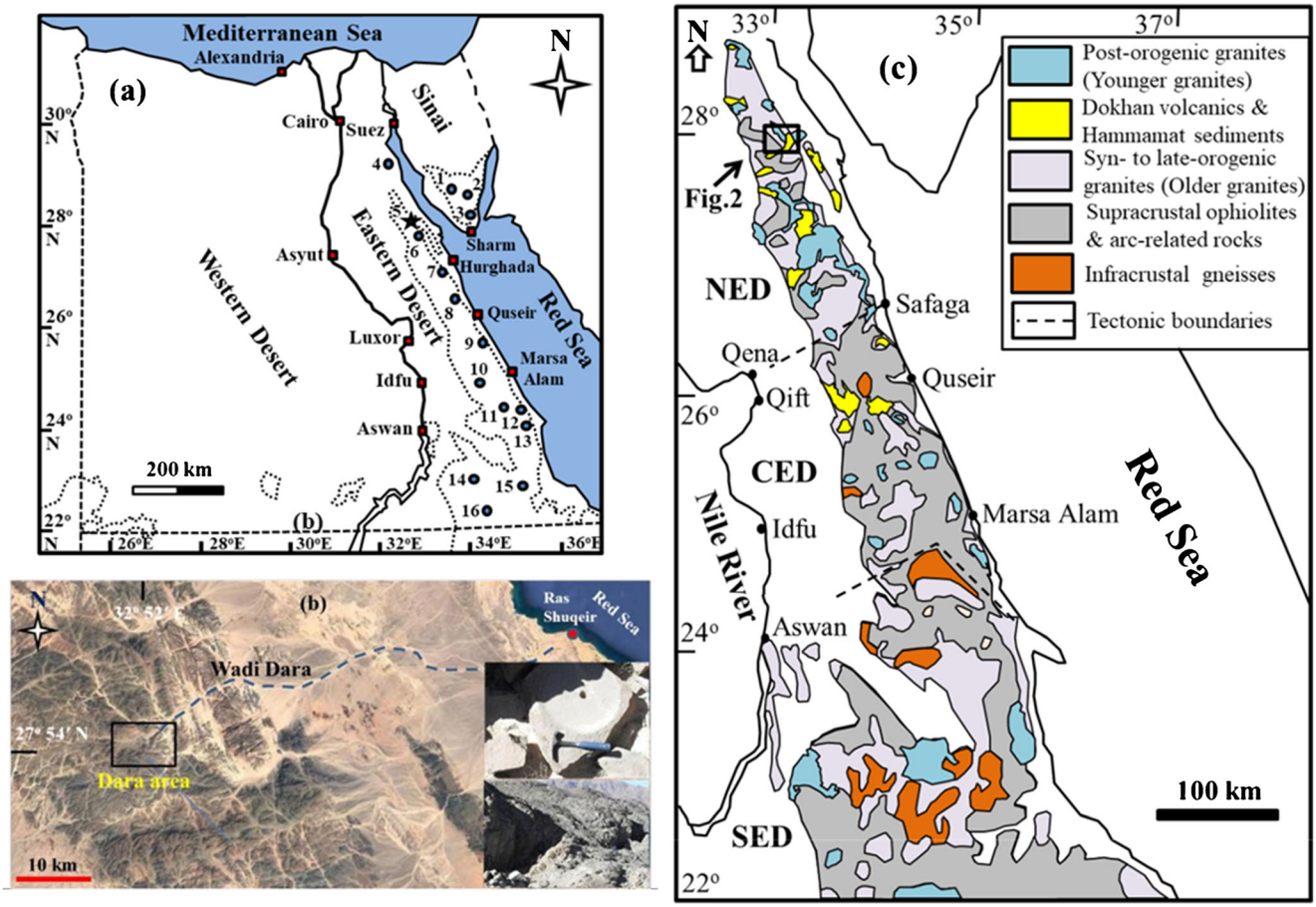


**Fig. 1** a Distribution of copper occurrences in Egypt: 1, Wadi Rofaiyed; 2, Regeita; 3, Samra; 4, Wadi Araba; 5, Dara; 6, Umm Mongul; 7, Humr Waggat; 8, Igla; 9, Zabara; 10, Muweilha; 11, Nugrus; 12, El Gharabiya; 13, Nikeiba; 14, Hamash; 15, Umm Samiuki; 16, Umm Garayat. Location of the study occurrence has the star symbol, b satellite image showing the location of the study area (marked rectangle), insets are milling stone and surface excavated sites observed at the Dara copper mine, c geologic map of the Eastern Desert of Egypt showing the main geotectonic units (After Ali et al. 2015) and tectonic boundaries (dashed lines, after Stern and Hedge 1985) between north, central, and southern Eastern Desert, symbolized as NED, CED, SED, respectively

In this paper, we present field, petrographic, and geochemical data on the Dara Cu mineralization and its host rocks, one of the controversial occurrences in the northern Eastern Desert of Egypt. The Dara area (~ 3 km$^2$) is located approximately 60 km west of Ras Shuqeir at the coast of the Red Sea, between latitudes 27° 54′ and 27° 55′N and longitudes 32° 51′ 30″ and 32° 52′ E (Fig. 1b). Dara copper mine is one of the oldest among the Egyptian mines that date back to the Roman time (Hussein 1990). Milling stones, surface excavated zones, and inclined shafts are still preserved near the old mine site (Fig. 1b). The Dara copper mineralization was suggested by Bishady et al. (2001) as a litho-tectonically controlled deposit related to within-plate magmatic activity. Al-Boghdady et al. (2003), based on a descriptive study of alteration paragenesis, suggested that the Dara mineralization represents a porphyry copper-related deposit. The geochronological study, carried out by Abdel Rahman and Doig (1987) on the dioritic rocks (gabbro-diorite, diorite, and porphyritic granodiorite) of the Dara area, has delineated ages of 881 ±58 Ma, 690 ±28 Ma, and 620 ±16 Ma for these rocks, respectively. An island arc tectonic setting was suggested for the Dara granitoid rocks by El-Desoky and Hafez (2018). The current study aims to characterize and quantify alteration patterns in the diorite and porphyritic granodiorite, the main host rocks of copper mineralization in the Dara area. The study aims also at constraining the characters of the Cu-mineralizing fluids and the physico-chemical conditions under which alteration and ore minerals have been precipitated. The genetic relation between the hydrothermal fluids and the host dioritic rocks was also discussed.

## Geological setting

The basement rocks of the Eastern Desert of Egypt belong to the Arabian-Nubian Shield (ANS), which represents along with the southeastern extension of the Mozambique Belt (MB) the Neoproterozoic crust that has been developed during

the East African orogeny (1000–541 Ma, Stern 2018). The ANS is composed of juvenile rock terranes of Tonian, Cryogenian, and Ediacaran ages (Greiling et al. 1994; Johnson et al. 2011; Fritz et al. 2013; Stern 2018). Five main tectonic units were identified and litho-stratigraphically arranged in the Eastern Desert of Egypt (Fig. 1c). These units arranged from bottom to top are (i) infracrustal gneisses and migmatites of high-grade metamorphism, (ii) supracrustal ophiolitic and arc-related rocks of low-grade metamorphism, (iii) syn- to late-orogenic Cryogenian I-type granites (referred to as older granites), (iv) late-orogenic intermediate to acidic volcanic rocks (Dokhan volcanics) and molasse-type sediments (Hammamat sediments), and (v) post-orogenic Ediacaran A-type granites (referred to as younger granites). Based on geographic distribution, structural patterns, and absolute ages of the abovementioned basement units, Stern and Hedge (1985) have subdivided the Egyptian Eastern Desert into three main terrains: northern Eastern Desert (NED), central Eastern Desert (CED), and southern Eastern Desert (SED). The NED is characterized by dominant post-collisional Dokhan volcanics, Hammamat sediments, and Ediacaran A-type younger granites. The CED is dominated by ophiolites and arc-related rocks of metavolcanic and metasediment varieties. The SED is characterized by abundant gneisses and migmatites (core complexes), less abundant ophiolites and arc-related rocks, and more abundant Cryogenian I-type older granites (Stern 2018 and references therein).

The Dara area is covered by metavolcanics, gabbro-diorite, older granites, Dokhan volcanics, Hammamat sediments, and younger granites (Fig. 2). The metavolcanic rocks are exposed in the northwestern and southern parts of the Dara area, covering about 10% of the total exposed rocks, and represent the oldest rock unit in the area. They are massive to weakly foliated, dark gray to yellowish green, and represented by meta-andesite and meta-rhyolite varieties. The gabbro-diorite is exposed as small masses in the southeastern part of the Dara copper mine site and has sharp intrusive contacts against the metavolcanic and granitic rocks (Fig. 2). Both gabbro-diorite and metavolcanics belong to the arc-related rocks of the NED, and both types are metamorphosed under greenschist facies conditions (Abdel Rahman and Doig 1987; Zaki 1996). Older granites are represented by greenish gray diorite and gray porphyritic granodiorite. Both units occur as discrete plutons of low relief and sharp contacts with surrounding rocks. The Dokhan volcanics constitute high mountainous exposures occupying the western part of the Dara area (Fig. 2). Greenish andesite and reddish dacite to rhyodacite, with common porphyritic texture, are the main varieties of the Dokhan volcanics. In the copper mine site, they surround the older granite against sharp contacts in a semi-circular pattern and are represented mainly by dacites and rhyodacite (Fig. 3). Hammamat sediments of green conglomerate and red siltstone varieties uncomfortably overlay the Dokhan volcanics in the northern and southern parts of the Dara area (Fig. 2). The Younger granitoids are the most abundant rock units at the Dara area constituting > 50% of the exposed rocks (Fig. 2). They comprise alkali feldspar granite, syenogranite, and monzogranite varieties (El-Desoky and Hafez 2018). In the copper mine site, syenogranite is the dominant granitic variety, which forms reddish mountainous exposure to the east of the copper old mine (Fig. 3).

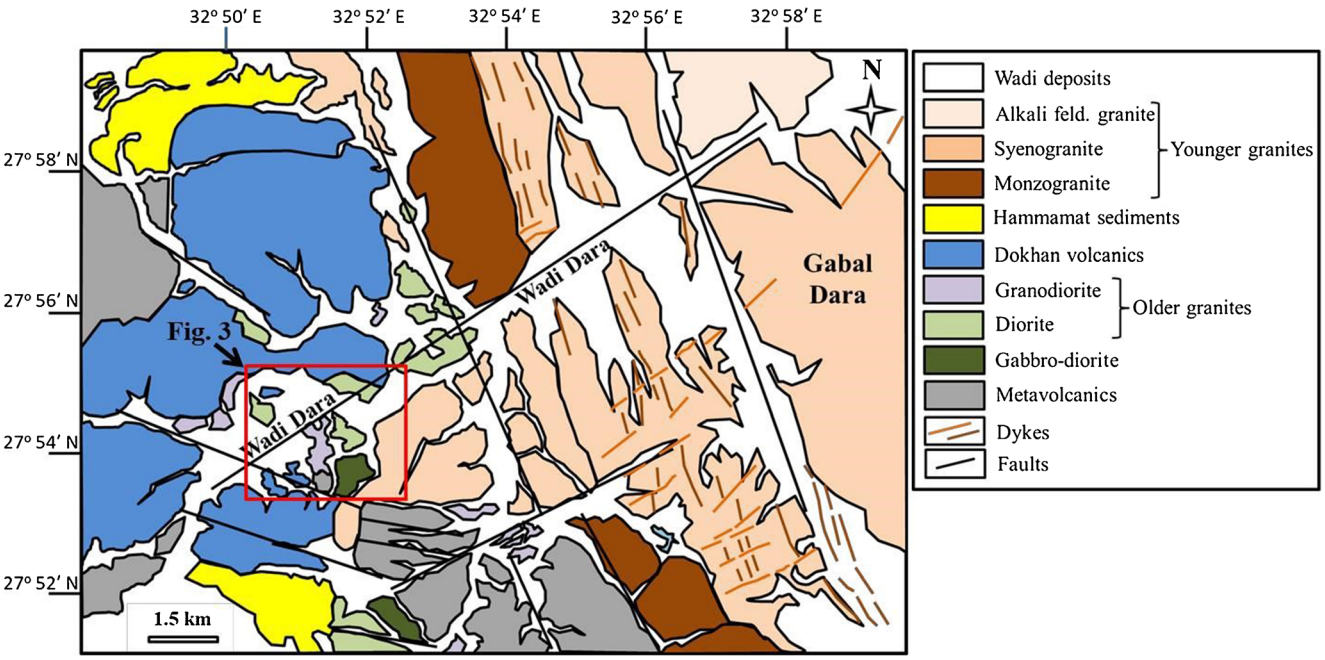


**Fig. 2** Geologic map of the Wadi Dara area, north Eastern Desert, Egypt (modified from Abdel Magid et al. 1998)

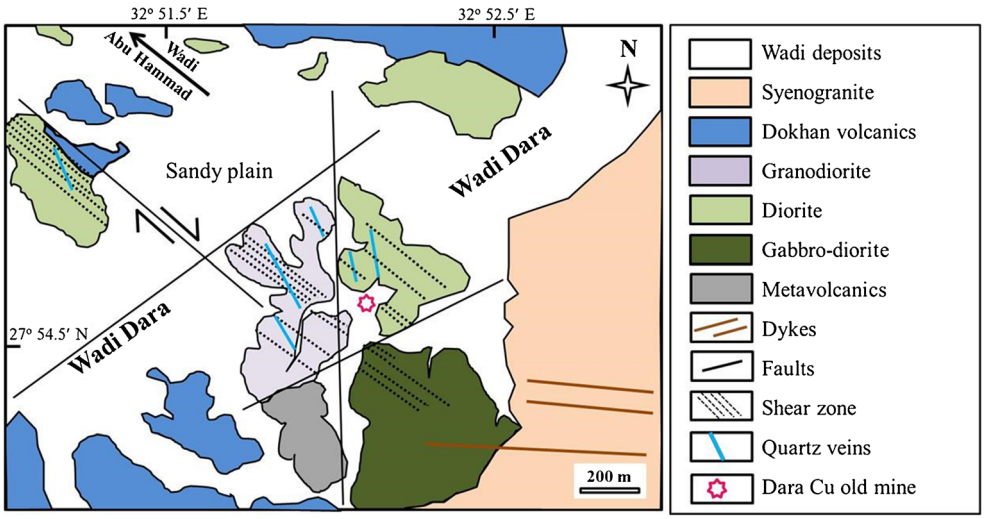


**Fig. 3** Detailed geologic map of the Dara copper mine area inset in Fig. 2

The structural elements of the Dara area are represented by a main NW shear zone and subordinate NE, ENE, N-S, and NNW fault planes (Fig. 3). The shear zone has an N 40° W trend and extends for about 5 km crosscutting the diorite and granodiorite rocks. It reaches up to 250 m in width in the mine site and contains all recognized mineralized quartz veins (Fig. 3). The area is dissected also by extensional fractures filled with different dike rocks especially in the eastern part of the Dara area. The crosscut relationship of the dike rocks revealed that the N-S trend is the youngest and ENE is the oldest one.

The Dara copper mineralization is exposed in six main mineralized quartz veins containing chalcopyrite, pyrite, and iron hydroxides hosted in the diorite and porphyritic granodiorite (Fig. 4a). All veins have a general NNW trend and range in thickness from 30 cm to 1.25 m of strike extension up to 400 m. They are included in the main shear zone that strikes

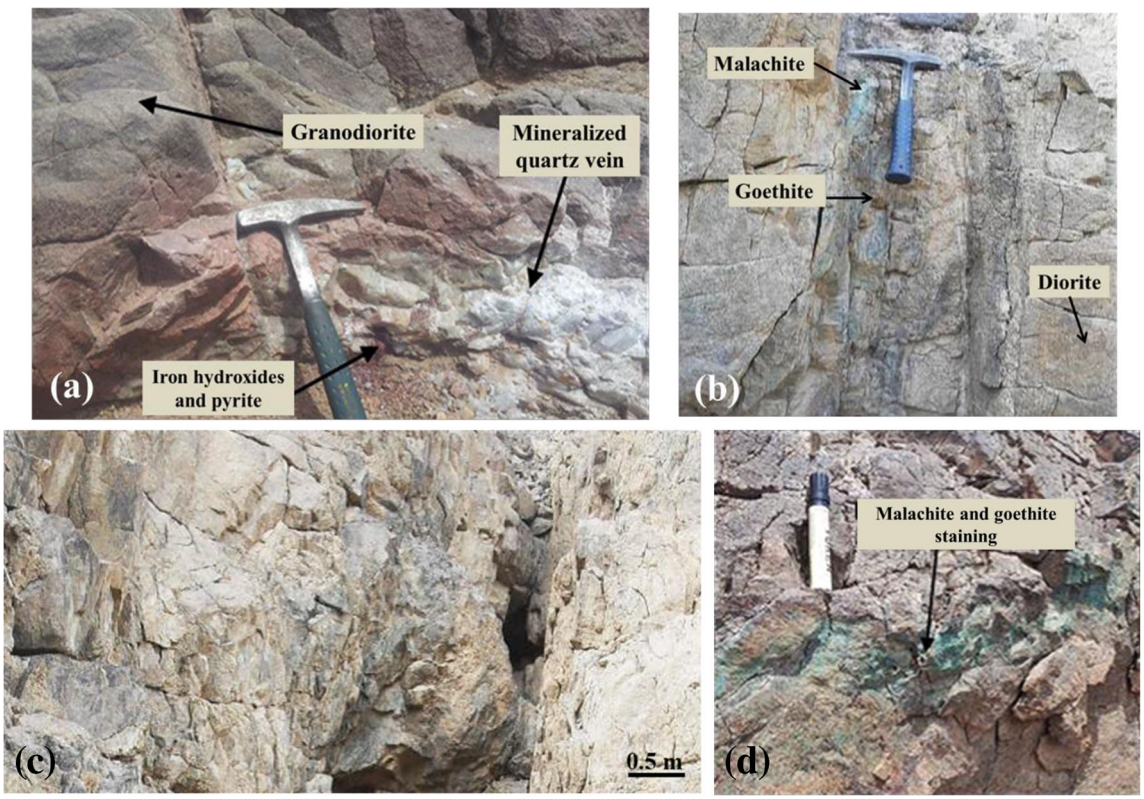


**Fig. 4** Field photographs showing the following: a Mineralized quartz vein invading granodiorite near the Dara old copper mine. b Malachite and goethite staining along sheared diorite, view looking NW. c View looking NNW along the Dara shear zone with sericite-pyrite alteration aureole reaches up to 4 m in width. d Malachite and goethite in sheared and altered granodiorite host, photo looking NE

NW and extends for 2 km. The sheared host rocks are extensively stained by malachite and goethite along their fracture planes (Fig. 4b). The mineralized veins are surrounded by alteration zones: reddish-white sericite-pyrite alteration zone near the veins and greenish chlorite-sericite alteration zone near the least altered rocks. The sericite-pyrite alteration zone ranges in thickness from 2 to 4 m and contains common Fe minerals (e.g., pyrite, magnetite) and subordinate Cu minerals (Fig. 4c). The chloritized zone is dominated by hematite. Supergene minerals (green malachite and reddish yellow goethite) are frequently encountered in the alteration zones (Fig. 4d).

## Investigative methodology

### Sampling and analytical techniques

A total of 50 samples representing fresh and altered granitoid rocks as well as mineralized quartz veins were collected from the study area. Based on the microscopic study of 40 thin and polished sections, 24 samples (11 from the least altered granitoid rocks and 13 from the altered ones) were chosen for major and selected trace element analyses. The chemical analysis was performed at the analytical laboratory of the Egyptian Mineral Resources Authority (EMRA) using X-ray fluorescence (Philips PW2404 Spectrometer) for major elements and inductively coupled plasma emission spectrometer (Agilent 720 ICP-OES) for trace element analyses. Fused sample disks (after mixing with lithium tetraborate flux) and international standards (BHVO-1, BCR-1, BIR-1) were used for determining and calibrating the XRF results. The precision was found to be within ± 4% for all major elements. Selected trace elements (Cu, Pb, Zn, Mo, Ni, Cr, Sr, Rb, and Y) were analyzed under the following conditions: RF power = 1.2 KW, nebulizer pressure = 200 KPa, nebulizer gas flow = 1.5 (L/min), and plasma gas flow = 15 (L/min). Standards prepared from certified reference materials were used for calibration and testing the accuracy of the ICP analysis. The detection limits of the selected elements are 0.4 ppm for Cu; 1 ppm for Pb; 0.2 ppm for Zn, Cr, and Y; 0.5 ppm for Mo and Ni; 0.05 ppm for Sr; and 5 ppm for Rb.

### Mass balance calculations

The current study of the alteration pattern is focused on the alteration zones derived from diorite and granodiorite, the main hosts of the mineralized quartz veins. To quantify alteration processes, different methods based on the mass transfer equation of Gresens (1967) have been suggested (e.g., Babcock 1973; Grant 1986; Leitch and Lentz 1994). Precursor composition and reliable monitor immobile element are the main requirements for performing mass balance calculations in all of these methods. In this study, we apply the method of Grant (1986), modified from the mass transfer equation of Gresens (1967) by replacing density variation with the chemical compositions of the altered rocks and their precursors. According to Grant (1986), a reference line corresponding to a zero concentration change (an isocon) is a graphical simultaneous solution of Gresens' equations for zero concentration change, so that the slope of the isocon can yield the mass and volume changes in the alteration. The gains and losses relative to concentrations in the original rock can then be calculated according to the following equation:

$$Xn = 100\ \{[(X_n^B)\ (Fv)] - X_n^A\}$$

where Xn is the loss or gain value of component n (expressed as grams per 100 g of parent rock); Fv is the volume factor, which can be obtained from composition-volume diagrams or calculated as $(X^A_{immobile}/X^B_{immobile})$; and $X_n^B$ and $X_n^A$ are the weight percentage of component "n" in altered rock and least altered rock obtained directly from chemical analyses, respectively. The least altered diorite and granodiorite identified in this study were used as the precursor rocks. For identifying the suitable immobile element that has not been modified by the alteration process, to be used for calibrating the mass balance calculations, the composition of altered rocks has been compared to that of their equivalent precursors (Supplementary Fig. 1). Accordingly, aluminum was selected as the most suitable immobile element for use in mass balance calculations. To determine volume factors (Fv) for the altered varieties of each zone, composition-volume diagrams were constructed (Supplementary Fig. 2), and the obtained Fv values were compared with those calculated by $X^A_{immobile}/X^B_{immobile}$; both results were turned out to be nearly identical.

## Mineralogy and petrography

### Least altered rocks

The least altered rocks are those in which distinct petrographic features related to the mineralizing event are minor or absent. Four main varieties of the least altered rocks were identified: gabbro-diorite, diorite, granodiorite, and granite. The gabbro-diorite is coarse-grained, meso- to melanocratic rock composed mainly of plagioclase (62% by mode, $An_{26–32}$), reddish brown oxyhornblende (21%), and clinopyroxene (9%, augite) and is characterized by equigranular and poikilitic texture (Fig. 5a). Magnetite is the main accessory opaque mineral, whereas chlorite and epidote are secondary minerals.

The diorite is mesocratic with medium-grained hypidiomorphic texture and contains plagioclase (65% by mode), hornblende (15%), K-feldspar (8%), quartz (9%), and biotite (2%) (Fig. 5b). The plagioclase crystals are of andesine composition ($An_{20–27}$) and are occasionally

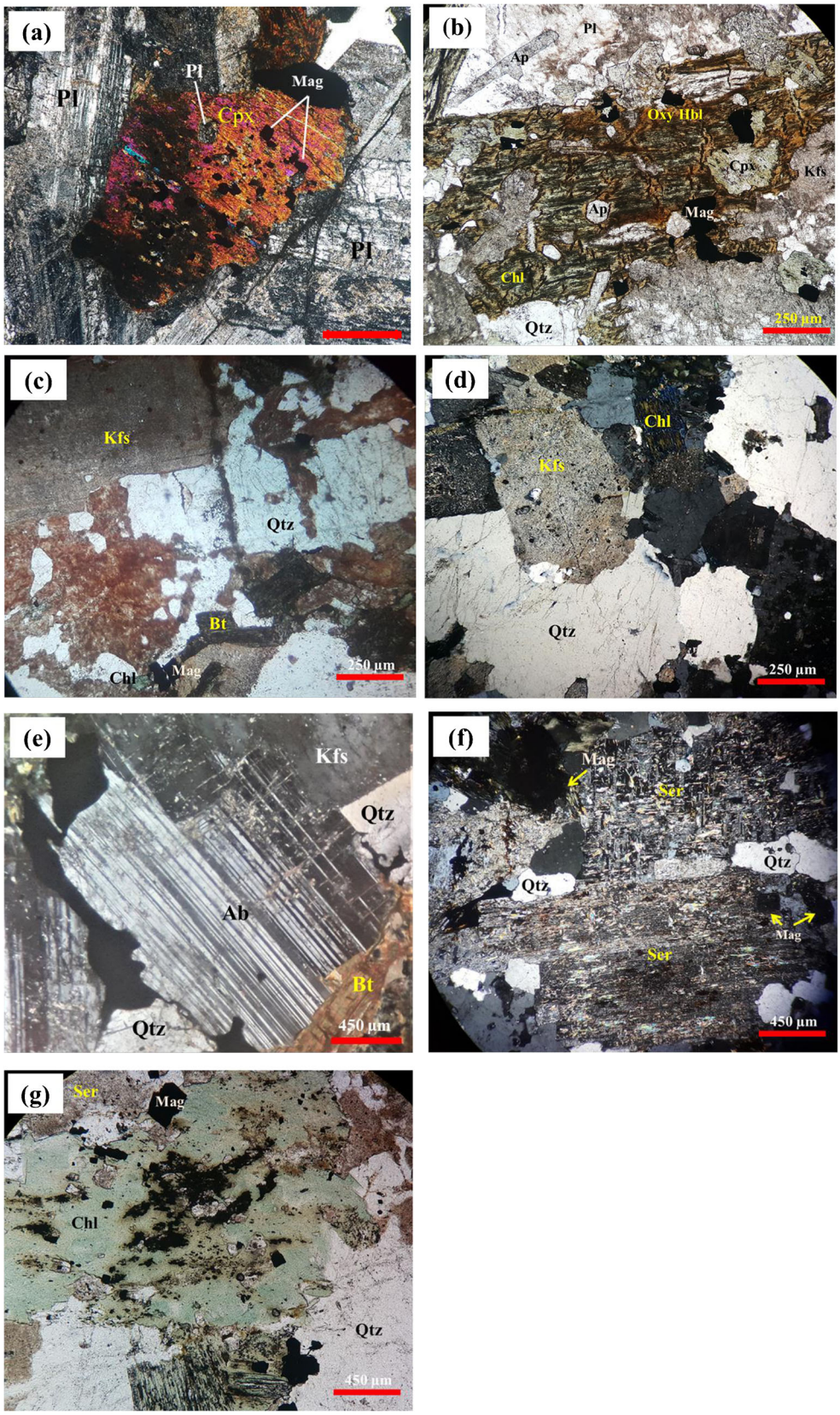


sericitized. Brown hornblende (oxy-hornblende) is the main mafic mineral and is variably altered to chlorite. K-feldspar, represented mainly by orthoclase, occurs as anhedral to subhedral crystals. Quartz generally occurs as interstitial

◀ **Fig. 5** Photomicrographs of least altered (a–e) and altered (f, g) rocks in the Dara copper mine area. a Clinopyroxene with inclusions of opaque minerals (magnetite) along with plagioclase in gabbro-diorite (XPL). b Slightly chloritized oxyhornblende with apatite and magnetite inclusions and surrounded by feldspars in the diorite variety (PPL). c K-feldspar and quartz phenocrysts, biotite relicts, chlorite, and magnetite in the granodiorite variety (XPL). d Granitic texture of quartz, K-feldspar, and biotite in the syenogranite variety (XPL). e Subhedral tabular albite and biotite in the syenogranite (XPL). f Sericite and magnetite in the sericite zone (in granodiorite) (XPL). g Chlorite and magnetite in the chlorite zone (in granodiorite host) (PPL). Abbreviations: apatite (Ap), biotite (Bt), chlorite (Chl), hornblende (Hbl), K-feldspar (Kfs), magnetite (Mag), orthoclase (Or), albite (Ab), plagioclase (Pl), clinopyroxene (Cpx), quartz (Qtz), sericite (Ser)

anhedral medium-grained crystals. Apatite and sphene are the main accessory minerals.

The granodiorite is composed essentially of plagioclase ($An_{10–16}$) and quartz with modal contents that reach up to 39% and 35%, respectively. K-feldspar (18%) and biotite (~ 6%) are less abundant (Fig. 5c). The rock is porphyritic with prismatic K-feldspar and plagioclase phenocrysts (up to 8 mm in length, of oligoclase/andesine composition) embedded in a fine-grained groundmass, which is composed of fine-grained feldspar, quartz, and traces of biotite. Zircon, apatite, and magnetite are common accessory minerals, whereas sericite and chlorite are the main secondary minerals.

The younger granite is composed of quartz (46% by mode) and K-feldspar (34%), along with less common plagioclase and minor biotite (Fig. 5d). The determined proportions of K-feldspar and plagioclase define the rock as syenogranite. The rock shows a medium-grained hypidiomorphic texture. Quartz generally occurs as interstitial anhedral crystals ranging in diameter from 3 to 5 mm. K-feldspar, mostly orthoclase, is of medium- to coarse-grained subhedral crystals showing simple Carlsbad twins. Plagioclase occurs as subhedral tabular crystals showing clear albite twins (Fig. 5e). Biotite exhibits subhedral flakes up to 2 mm in length and is occasionally chloritized. Zircon and iron oxides are common accessory minerals.

## Altered rocks

The mineralogical and textural features of the investigated altered rocks are characterized by two genetically different mineral associations: (a) those formed by supergene alteration containing abundant malachite and goethite, which are out of the scope of this study, and (b) those formed through the effect of hydrothermal activity, which will be described below. The hydrothermal alteration resulted in developed two alteration zones around the mineralized quartz veins. These are (i) sericite-pyrite assemblage and (ii) chlorite-sericite assemblage.

(i) **Sericite-pyrite assemblage (sericite zone)** is made up of sericite (up to 60% by mode), pyrite, magnetite, and minor chlorites. Sericite replaces plagioclase and K-feldspar and sometimes forms pseudomorphic texture after feldspars (Fig. 5f). The sericite pseudomorphs retain the porphyritic texture in the granodiorite variety. Fine-grained pyrite and magnetite are the main ore mineral identified in this assemblage. Minor chlorite, after hornblende and biotite, was also identified.

(ii) **Chlorite-sericite assemblage (chlorite zone)** is composed of chlorite (up to 57% by mode), sericite (up to 15%), hematite, and minor magnetite. Chlorite replaces hornblende in diorite and partially replaces biotite and/or K-feldspar in granodiorite (Fig. 5g). Sericite is less abundant and occurs commonly as an alteration product of feldspar. Hematite and minor magnetite are the main ore minerals.

## Quartz veins and ore minerals

The quartz veins consist mainly of quartz (> 90% by mode). The quartz crystals are medium- to fine-grained that show sutured boundaries forming a granular mosaic texture (Fig. 6a). Wavy extinction, cracks, and brecciation are common in most of the quartz crystals indicating deformation and subsequent crystallization of quartz. Pyrite, chalcopyrite, pyrrhotite, covellite, hematite, goethite, and malachite are the main ore minerals that are sporadically disseminated in the mineralized quartz veins and alteration zones. Pyrite is the most common sulfide mineral, which occurs in three distinct types based on optical properties and textural relationships: (i) fine-grained clustered anhedral to subhedral crystals in quartz veins (Fig. 6b); (ii) fine-grained, euhedral and subhedral crystals commonly associated with magnetite in the sericite alteration zone (Fig. 6c); and (iii) subhedral medium-grained crystals containing xenomorphic inclusions of pyrrhotite (Fig. 6d) in the sericite alteration zone. Covellite after chalcopyrite and malachite is commonly observed in the quartz veins and the sericite alteration zone (Fig. 6e). Oxide minerals are represented by magnetite and hematite. Magnetite occurs as euhedral to subhedral crystals in host rocks and alteration zones, more abundant in the sericite one, where it is partly to completely martitized (Fig. 6f, g). By contrast, hematite and goethite are the main ore minerals in the chlorite zone.

# Geochemical results and interpretation

The chemical analysis of 24 samples representing the least altered and altered rocks is given in Tables 1 and 2. Alteration index (AI) of Ishikawa et al. (1976) and chlorite-

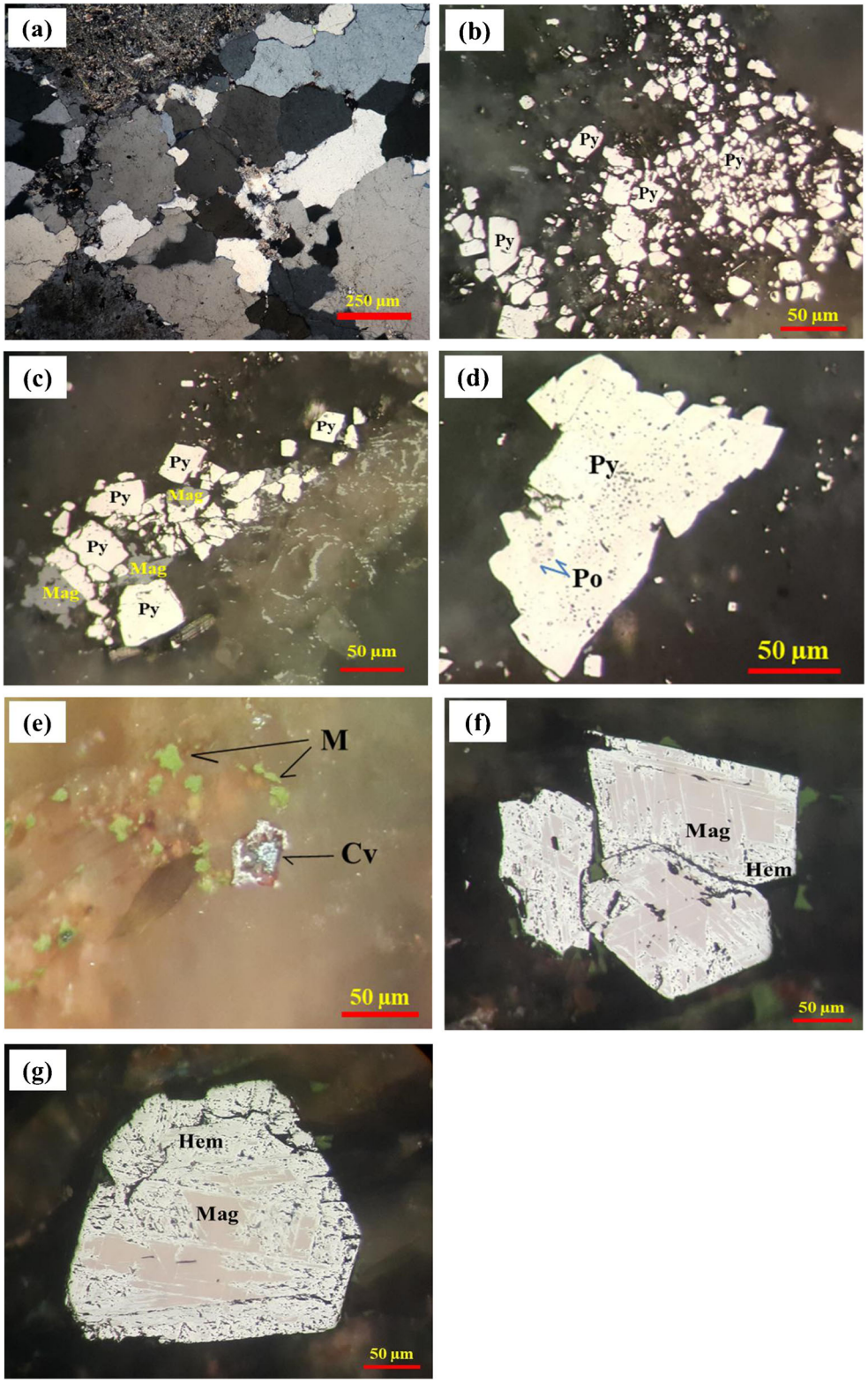


**Fig. 6** Photomicrographs showing quartz vein and ore minerals in the Dara copper mine area. a Quartz vein containing disseminated ore minerals (black crystals) adjusting sericite zone in granodiorite (XPL). (b–g) Reflected light photomicrographs showing b cluster of fine subhedral pyrite grains in quartz vein, c fine-grained euhedral pyrite crystals associated with magnetite (Mag) in quartz veins in the diorite host rock; d pyrite (Py) most probably after pyrrhotite (Po, relics in pyrite) in the sericite zone, e covellite (Cv) and malachite (M) in sericitized granodiorite, (f, g) partly to severely martitized magnetite in the altered diorite rock (Hem, hematite)

carbonate-pyrite index (CCPI) of Large et al. (2001) were calculated for the analyzed samples. Samples of AI > 60% and CCPI > 50% as recommended by Mathieu (2018) were considered as altered ones. The discrimination between the least altered and altered samples was confirmed by using AI and CCPI diagrams (Fig. 7).

**Table 1** Major oxide (wt.%) and selected trace element (ppm) concentrations of least altered granitoid rock units in the Dara area

| | Gabbro-diorite | | | | Diorite | | | | Granodiorite | | | | Granite | | | Clarke* |
|---|---|---|---|---|---|---|---|---|---|---|---|---|---|---|---|---|
| Sample no | m21 | m25 | Average | m22 | m24 | Average | m3 | m10 | m16 | m30 | Average | m11 | m12 | m13 | Average | |
| $SiO_2$ | 55.07 | 55.15 | 55.11 | 56.20 | 56.14 | 56.17 | 65.14 | 66.61 | 67.10 | 67.25 | 66.53 | 72.52 | 74.06 | 73.90 | 73.49 | 61.50 |
| $TiO_2$ | 1.03 | 1.07 | 1.05 | 1.05 | 1.16 | 1.11 | 0.51 | 0.50 | 0.52 | 0.63 | 0.54 | 0.10 | 0.12 | 0.09 | 0.10 | 0.68 |
| $Al_2O_3$ | 13.30 | 13.45 | 13.38 | 13.81 | 13.56 | 13.69 | 13.75 | 13.95 | 14.09 | 14.15 | 13.99 | 13.96 | 13.03 | 12.97 | 13.32 | 15.10 |
| FeO | 7.45 | 7.78 | 7.62 | 6.97 | 7.05 | 7.01 | 2.74 | 2.75 | 2.74 | 3.30 | 2.88 | 0.45 | 0.61 | 0.54 | 0.53 | 5.65 |
| MnO | 0.15 | 0.17 | 0.16 | 0.15 | 0.16 | 0.16 | 0.10 | 0.07 | 0.06 | 0.06 | 0.07 | 0.02 | 0.02 | 0.02 | 0.02 | 0.10 |
| MgO | 6.37 | 6.35 | 6.36 | 6.92 | 7.20 | 7.06 | 2.42 | 3.20 | 2.83 | 2.81 | 2.82 | 0.28 | 0.23 | 0.23 | 0.25 | 3.70 |
| CaO | 6.83 | 7.71 | 7.27 | 6.97 | 7.63 | 7.30 | 2.43 | 2.27 | 1.90 | 1.96 | 2.14 | 0.92 | 1.09 | 0.87 | 0.96 | 5.50 |
| $Na_2O$ | 2.59 | 3.01 | 2.80 | 2.95 | 2.74 | 2.85 | 3.22 | 3.65 | 3.79 | 3.40 | 3.52 | 2.95 | 3.01 | 3.20 | 3.05 | 3.20 |
| $K_2O$ | 1.71 | 1.56 | 1.64 | 1.59 | 1.45 | 1.52 | 4.23 | 4.55 | 5.05 | 3.82 | 4.41 | 7.22 | 6.67 | 5.90 | 6.60 | 2.40 |
| $P_2O_5$ | 0.26 | 0.25 | 0.26 | 0.27 | 0.30 | 0.29 | 0.17 | 0.15 | 0.15 | 0.19 | 0.17 | 0.03 | 0.03 | 0.03 | 0.03 | 0.18 |
| LOI** | 3.91 | 2.20 | 3.06 | 1.73 | 1.24 | 1.49 | 3.17 | 1.50 | 0.86 | 1.96 | 1.87 | 0.98 | 0.58 | 1.75 | 1.10 | 1.99 |
| Total | 98.67 | 98.70 | 98.69 | 98.61 | 98.63 | 98.62 | 97.88 | 99.20 | 99.09 | 99.53 | 98.93 | 99.43 | 99.45 | 99.50 | 99.46 | 100 |
| Cu | 9211 | 4863 | 7037 | 180 | 116 | 148 | 160 | 353 | 165 | 402 | 270 | 187 | 116 | 148 | 150 | 55 |
| Pb | 5.1 | 5.5 | 5.3 | 4.3 | 5.0 | 4.7 | 11.0 | 5.7 | 12.0 | 4.0 | 8.2 | 2.0 | 11.2 | 6.0 | 6.4 | 15 |
| Zn | 85 | 83 | 84 | 68 | 80 | 74 | 64 | 28 | 66 | 65 | 56 | 7 | 6 | 73 | 29 | 65 |
| Mo | 1.5 | 1.5 | 1.5 | 2.5 | 2.0 | 3.0 | 6.0 | 3.0 | 6.0 | 1.0 | 4.0 | 1.0 | 2.5 | 3.6 | 1.8 | 1.5 |
| Ni | 46 | 61 | 53 | 49 | 56 | 53 | 250 | 32 | 100 | 180 | 140 | 13 | 24 | 51 | 29 | 56 |
| Cr | 91 | 90 | 90 | 75.3 | 93 | 84 | 100 | 64 | 180 | 120 | 116 | 16 | 22.8 | 46 | 28 | 126 |
| Rb | 170 | 68 | 119 | 150 | 101 | 126 | 41 | 111 | 115 | 133 | 100 | 133 | 118 | 113 | 121 | 78 |
| Sr | 68 | 162 | 115 | 89 | 159 | 124 | 55 | 189 | 109 | 109 | 116 | 112 | 157 | 159 | 143 | 333 |
| Y | 60 | 29 | 45 | 66 | 44 | 55 | 44 | 28 | 27 | 27 | 31 | 25 | 27 | 22 | 25 | 24 |

*Average upper continental crust after Wedepohl (1995)

**Loss on ignition

**Table 2** Major oxide (wt.%) and selected trace element (ppm) concentrations of altered rock units in the Dara area

| | Sericite zone | | | | | | | | Chlorite zone | | | | | | | | |
|---|---|---|---|---|---|---|---|---|---|---|---|---|---|---|---|---|---|
| Sample | | | Diorite | | | Granodiorite | | | | | Diorite | | | | Granodiorite | | |
| no | m20 | m33 | m34 | m35 | Average | m4 | m15 | Average | m1 | m6 | m7 | m23 | Average | m8 | m17 | m18 | Average |
| $SiO_2$ | 55.18 | 60.75 | 58.34 | 61.04 | 58.83 | 65.04 | 65.84 | 65.44 | 55.69 | 57.02 | 59.75 | 56.31 | 57.19 | 72.26 | 66.75 | 66.24 | 68.42 |
| $TiO_2$ | 1.42 | 0.97 | 1.00 | 0.80 | 1.05 | 0.68 | 0.56 | 0.62 | 1.05 | 1.15 | 0.89 | 1.14 | 1.06 | 0.41 | 0.63 | 0.66 | 0.57 |
| $Al_2O_3$ | 19.17 | 12.40 | 14.48 | 17.07 | 15.78 | 13.16 | 14.58 | 13.87 | 13.75 | 14.55 | 13.15 | 14.35 | 13.95 | 11.90 | 15.04 | 14.95 | 13.96 |
| FeO | 7.85 | 7.20 | 7.89 | 6.04 | 7.25 | 4.09 | 3.46 | 3.77 | 8.09 | 8.07 | 6.54 | 8.56 | 7.82 | 2.44 | 3.28 | 3.69 | 3.14 |
| MnO | 0.01 | 0.20 | 0.05 | 0.05 | 0.08 | 0.10 | 0.05 | 0.08 | 0.15 | 0.14 | 0.15 | 0.17 | 0.15 | 0.06 | 0.05 | 0.06 | 0.06 |
| MgO | 1.06 | 1.15 | 0.88 | 1.30 | 1.10 | 3.06 | 2.65 | 2.86 | 6.99 | 6.91 | 5.94 | 7.24 | 6.77 | 2.05 | 2.49 | 2.65 | 2.40 |
| CaO | 0.49 | 0.36 | 1.43 | 0.69 | 0.74 | 1.81 | 0.67 | 1.24 | 1.87 | 1.30 | 1.15 | 1.51 | 1.46 | 1.01 | 0.96 | 0.81 | 0.93 |
| $Na_2O$ | 1.88 | 1.32 | 1.17 | 1.45 | 1.46 | 2.76 | 3.46 | 3.11 | 2.85 | 4.17 | 3.71 | 3.14 | 3.47 | 2.99 | 3.31 | 3.74 | 3.35 |
| $K_2O$ | 4.81 | 7.70 | 5.87 | 6.05 | 6.11 | 5.53 | 4.49 | 5.01 | 1.96 | 1.78 | 2.40 | 1.90 | 2.01 | 5.01 | 5.38 | 4.88 | 5.09 |
| $P_2O_5$ | 0.15 | 0.09 | 0.10 | 0.09 | 0.11 | 0.21 | 0.14 | 0.18 | 0.20 | 0.29 | 0.19 | 0.20 | 0.22 | 0.11 | 0.16 | 0.17 | 0.15 |
| LOI | 6.40 | 6.60 | 6.51 | 4.65 | 6.04 | 2.40 | 2.81 | 2.61 | 5.51 | 4.44 | 4.54 | 4.46 | 4.74 | 0.99 | 2.01 | 1.14 | 1.38 |
| Total | 98.42 | 98.74 | 97.72 | 99.23 | 98.53 | 98.84 | 98.71 | 98.77 | 98.11 | 99.82 | 98.41 | 98.98 | 98.83 | 99.23 | 100.06 | 98.99 | 99.43 |
| AI* | 71.24 | 84.05 | 72.19 | 77.45 | 76.23 | 65.27 | 63.35 | 64.31 | 65.47 | 61.37 | 63.18 | 66.28 | 64.08 | 63.83 | 64.83 | 62.33 | 63.67 |
| CCPI** | 78.99 | 83.25 | 77.14 | 77.42 | 79.20 | 61.02 | 59.65 | 60.33 | 76.16 | 73.26 | 71.98 | 77.26 | 74.66 | 52.88 | 57.47 | 58.22 | 56.19 |
| Cu | 8016 | 15166 | 23660 | 7399 | 13560 | 14460 | 147 | 7304 | 72 | 8800 | 10806 | 149 | 4956 | 74.3 | 633 | 4160 | 1622 |
| Pb | 18 | 2 | 21 | 15 | 14 | 72 | 8 | 40 | 11 | 6 | 16 | 7 | 10 | 4 | 5 | 6 | 5 |
| Zn | 44 | 56 | 59 | 37 | 49 | 100 | 48 | 74 | 64 | 61 | 100 | 66 | 73 | 29 | 53 | 63 | 48 |
| Mo | 175 | 4 | 10 | 12 | 50 | 130 | 2 | 66 | 6 | 60 | 7 | 1 | 19 | 3 | 11 | 3 | 6 |
| Ni | 7 | 38 | 360 | 28 | 108 | 78 | 89 | 84 | 124 | 350 | 300 | 153 | 232 | 44.2 | 97 | 34 | 59 |
| Cr | 52 | 29 | 47 | 34 | 41 | 8 | 9 | 9 | 100 | 180 | 76 | 120 | 119 | 68 | 150 | 58 | 92 |
| Rb | 99 | 63 | 21 | 15 | 49 | 72 | 75 | 74 | 23 | 29 | 65 | 168 | 71 | 100 | 67 | 86 | 84 |
| Sr | 175 | 189 | 214 | 196 | 194 | 65 | 201 | 133 | 60 | 60 | 91 | 142 | 88 | 105 | 159 | 162 | 142 |
| Y | 44 | 26 | 33 | 35 | 35 | 39 | 29 | 34 | 40 | 42 | 26 | 48 | 38 | 28 | 24 | 22 | 25 |

*Alteration index of Ishikawa et al. (1976)

**Chlorite-carbonate-pyrite index of Large et al. (2001)

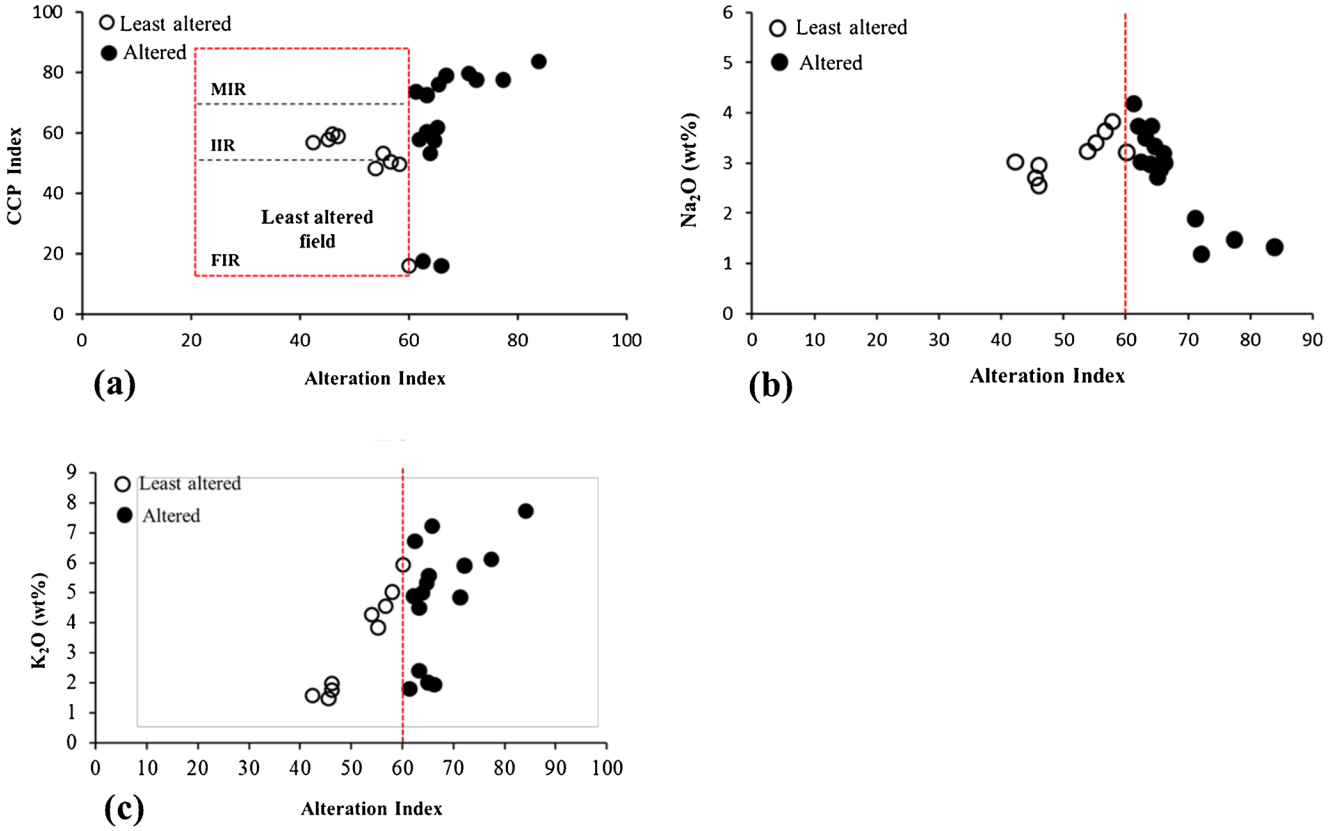


**Fig. 7** The plot of the Dara granitoid rocks in alteration discriminating diagrams. a Alteration index (AI) vs. chlorite-carbonate-pyrite index (CCPI) diagram (alteration box plot of Large et al. 2001). The fields for least altered felsic (FIR), intermediate (IIR), and mafic (MIR) igneous rocks are from Gifkins et al. (2006) b Alteration index against $Na_2O$. c Alteration index against $K_2O$

## Least altered rocks

The least altered rocks range in composition from gabbro-diorite (55.11 wt.% $SiO_2$ on average) through diorite (56.17 wt.% $SiO_2$ on average) and granodiorite (66.53 wt.% $SiO_2$ on average) to granite (73.49 wt.% $SiO_2$ on average) and fall within the sub-alkaline field on the total alkali versus silica diagram of Le Maitre et al. (2002) (Fig. 8a). When normalized against the average composition of the upper continental crust (Clarke values of Wedepohl 1995), the gabbro-diorite variety revealed the highest content of Cu (7037 ppm on average) (Table 1, Fig. 8b). It also has higher contents of $TiO_2$, FeO, MnO, MgO, CaO, and Y and lower contents of $K_2O$, Pb, and Sr. The diorite has similar geochemical differences with Clarke values that characterize the gabbro-diorite rocks. However, the diorite has lower contents of FeO, MnO, CaO, and Cu compared to the gabbro-diorite variety. By contrast, the granodiorite and granite have higher contents of $K_2O$ and Cu and lower contents of FeO, MgO, CaO, and Sr and comparable contents of $Na_2O$ and Rb compared with Clarke values (Fig. 8b). The granodiorite, however, has distinctly higher contents of FeO, MnO, MgO, CaO, and $Na_2O$ and trace element contents compared with the granite (Table 1). The distinct high concentration of copper recorded in the least altered gabbro-diorite rock (Fig. 8b) may indicate that it could be a potential source of copper in the mine area.

All of the investigated granitoid rocks have a calc-alkaline affinity with FeO/MgO > 1.1 at a given $SiO_2$ content (Fig. 8c). The gabbro-diorite and diorite exhibit strong metaluminous nature, whereas granodiorite and granite reveal mild metaluminous affinity (Fig. 8d). The alumina saturation indices (ASI) are 0.68, 0.7, 0.97, and 0.96 on average for the gabbro-diorite, diorite, granodiorite, and granite, respectively. On the $SiO_2$ versus $K_2O$ diagram (Fig. 8e) of Peccerillo and Taylor (1976), the least altered granitoids are comparable with the medium-K and high-K series; the gabbro-diorite and diorite belong to the medium-K series, whereas the granodiorite and granite pertain to the high-K one; the latter is characterized by much more $K_2O$ content. Tectonically, the investigated gabbro-diorite and diorite fall within the mantle fractionate field, whereas granodiorite and granite are of pre- to syn-collision setting (Fig. 8f).

## Alteration geochemistry

The chemical composition of the alteration zones, developed in the diorite and granodiorite rocks that host the mineralized quartz veins, is listed in Table 2. Sericitization and chloritization trends, toward $K_2O$ apex and MgO apex, respectively, can be traced on

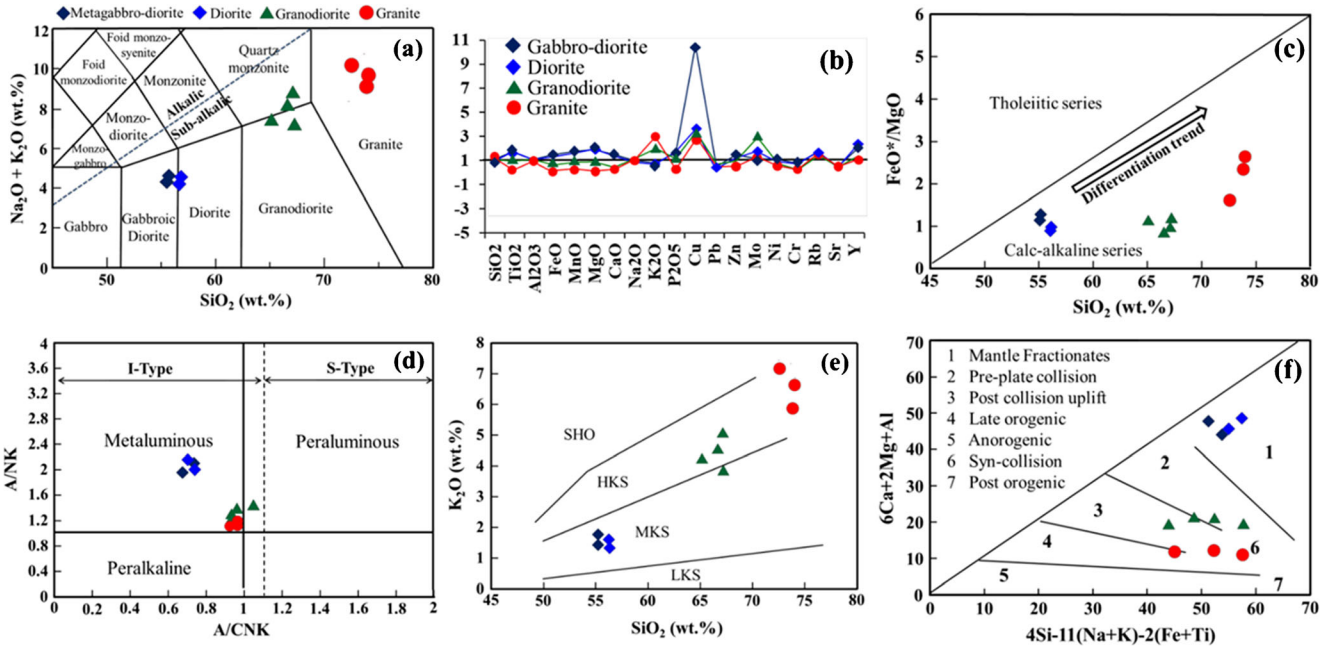


**Fig. 8** Geochemical classification, affinity, and tectonic setting of the Dara granitoid rocks shown on a total alkali versus silica diagram ($Na_2O+K_2O$ versus $SiO_2$; Le Maitre et al. 2002), the alkalic/sub-alkalic boundary from Irvine and Baragar (1971). b Upper continental crust-normalized spider diagram for major oxides and selected trace elements. c FeO/MgO vs. $SiO_2$ diagram of Miyashiro (1974). d A/CNK versus A/NK diagram after Maniar and Piccoli (1989); dashed line represents the boundary between I- and S-type granitoids after Chappell and White (1992). e $K_2O$ versus $SiO_2$ diagram (Peccerillo and Taylor 1976). Abbreviations: SHO, shoshonite series; HKS, high-K calc-alkaline series; MKS, medium-K calc-alkaline series; LKS, low-K calc-alkaline series. f R1 (4Si-11(Na+K)-2(Fe+Ti)) vs. R2 (6Ca+2Mg+Al) tectonic discrimination diagram of Batchelor and Bowden (1985)

the CaO-$K_2O$-MgO ternary diagram (Fig. 9). Loss-gain values of the sericite (sericite-pyrite) and chlorite (chlorite-sericite) alteration zones developed in the target host rocks were calculated for major and trace elements (Tables 3 & 4, Figs. 10 & 11). The obtained loss-gain values of the major elements (Table 3) can be represented by the following equations (LAR, least altered rock; AR, altered rock):

1. Sericitized diorite: 100gm LAR + 3.78 $K_2O$ + 1.16 L.O.I = 84.63 gm AR + 5.15 $SiO_2$ + 0.81 $Fe_2O_3$ + 6.11 MgO + 6.66 CaO + 1.58 $Na_2O$ ——— (1)
2. Sericitized granodiorite: 100gm LAR + 0.64 $K_2O$ + 0.06 MgO + 1.02 $Fe_2O_3$ + 0.76 L.O.I = 100.67 gm AR + 0.54 $SiO_2$ + 0.89 CaO + 0.38 $Na_2O$ ——— (2)
3. Chloritized diorite: 100gm LAR + 0.13 MgO + 0.29 $K_2O$ + 0.52 $Na_2O$ + 0.05 L.O.I = 94.71 gm AR + 0.27 $SiO_2$ + 0.14 $Fe_2O_3$ + 5.87 CaO ——— (3)
4. Chloritized granodiorite: 100gm LAR + 2.04 MgO + 2.73 $Fe_2O_3$ + 0.14 $Na_2O$ + 0.21 L.O.I = 95.07 gm AR + 8.23 $SiO_2$ + 1.74 $K_2O$ + 0.08 CaO ——— (4)

Generally, as shown in Table 3, the overall volume change in the sericite zone is more than that recorded in the chlorite one (being −11.96 % and 3.16 % in the sericitized diorite and granodiorite, respectively, and −3.41 % and −2.38 % in the chloritized diorite and granodiorite, respectively). This reflects the higher effectiveness of hydrothermal solutions on the sericite alteration zone.

The notable losses of Si and Ca in both zones are concomitant with the breakdown of plagioclase feldspar during the

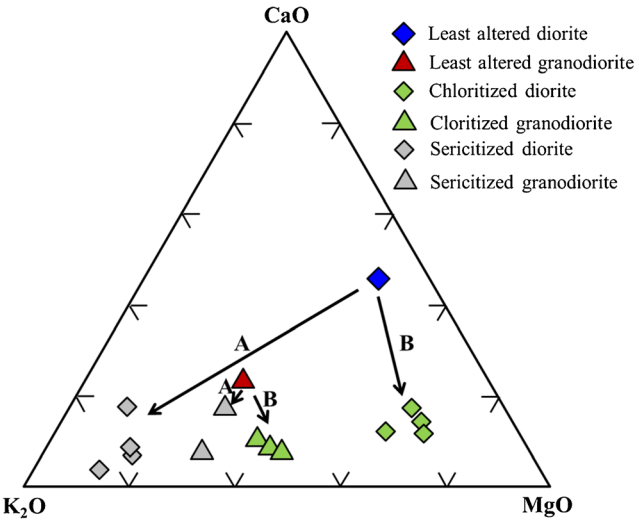


**Fig. 9** Average composition of least altered diorite and granodiorite from the Dara copper mine area plotted on the $K_2O$-CaO-MgO ternary diagram. Trends A and B represent sericitization and chloritization, respectively

**Table 3** Average gain or loss of major oxides (wt. %) in the sericite and chlorite alteration zones recognized in the diorite and granodiorite host rocks in the Dara copper mine area

| | Gain/loss in wt.% | | | |
|---|---|---|---|---|
| Oxide (wt.%) | Sericite zone | | Chlorite zone | |
| | Diorite | Granodiorite | Diorite | Granodiorite |
| $SiO_2$ | −5.15 | −0.54 | −0.27 | −8.23 |
| $Al_2O_3$ | 0.00 | 0.00 | 0.00 | 0.00 |
| $Fe_2O_3$ | −0.81 | 1.02 | −0.14 | 2.73 |
| MgO | −6.11 | 0.06 | 0.13 | 2.04 |
| CaO | −6.66 | −0.89 | −5.87 | −0.08 |
| $Na_2O$ | −1.58 | −0.38 | 0.52 | 0.14 |
| $K_2O$ | 3.78 | 0.64 | 0.29 | −1.74 |
| L.O.I | 1.16 | 0.76 | 0.05 | 0.21 |
| Average Fv* | 0.88 | 1.03 | 0.97 | 0.98 |
| Vol. change (%) | −11.96 | 3.16 | −3.41 | −2.38 |
| Mass change (%) | −15.37 | 0.67 | −5.29 | −4.93 |

*Fv is the volume factor calculated for each variety in alteration zones based on composition-volume diagrams

sericitization process. Magnesium and to a less extent Fe are removed in the sericitized diorite (Eq. 1) most probably due to the breakdown of ferromagnesian minerals. However, Mg and Fe are slightly added to the sericitized granodiorite (Eq. 2), maybe to form Mg and Fe minerals such as chlorite and magnetite; both minerals were microscopically identified. Sodium is slightly subtracted in the proximal sericite alteration zone and added to the distal chlorite one indicating the high mobility of Na in hydrothermal fluids. In the sericite alteration zones, K is strongly gained in the zone developed from diorite rather than from granodiorite (Table 3). The addition of K is controlled by sericitization of feldspar minerals where sericite modal % in sericitized diorite is higher than that in sericitized granodiorite. Consequently, it seems that plagioclase feldspars that constitute the major components in diorite were affected by sericitization as compared to K-feldspars which form the major minerals in granodiorite. In the chlorite alteration zones, on the other hand, K is added to the chloritized diorite (Eq. 3) but subtracted from chloritized granodiorite (Eq. 4). This difference may be due to the way by which sericite was formed in the chlorite alteration zone of these rock varieties (discussed below). Sodium, leached out from the proximal sericitized zone (Eq. 2) is added to the chlorite zones (i.e., chloritized diorite and chloritized granodiorite) (Table 3, Fig. 10, and mass balance equations). The significant Fe gain in the altered granodiorite rock (Eqs. 2 and 4) may be reflected in the formation of Fe-bearing sulfides (e.g., pyrite) and Fe oxides (e.g., magnetite); both minerals are abundant in altered granodiorite.

Regarding trace elements (Table 4), Rb (partitioned mainly in feldspar) was found to be leached from all zones during alteration processes reflecting the breakdown of feldspars. In contrast, Mo was added to all zones indicating its relatively high concentrations in the hydrothermal fluids (Fig. 11). Copper was found to be added only to the sericite zone developed in the diorite at the vicinity of quartz veins. However, copper is subtracted from the chlorite zone and sericitized granodiorite under low $K^+$ and $H^+$ activities (discussed below).

**Table 4** Average gain or loss of selected trace elements (ppm) in the sericite and chlorite alteration zones recognized in the diorite and granodiorite host rocks in the Dara copper mine area

| | Gain/loss in ppm | | | |
|---|---|---|---|---|
| Element | Sericite zone | | Chlorite zone | |
| | Diorite | Granodiorite | Diorite | Granodiorite |
| Rb | −82.68 | −25.89 | −50.69 | −40.89 |
| Sr | 43.81 | 18.60 | −30.39 | −7.21 |
| Pb | 7.37 | 32.17 | 4.24 | −1.61 |
| Zn | −31.54 | 18.86 | −14.40 | 17.41 |
| Cr | −49.03 | −107.45 | 23.79 | 59.24 |
| Ni | 41.18 | −56.21 | 169.10 | 26.54 |
| Cu | 11649 | −548 | −2279 | −4051 |
| Mo | 41.11 | 62.66 | 16.26 | 3.68 |
| Y | −25.08 | 3.03 | −7.11 | −1.14 |
| Average Fv* | 0.88 | 1.03 | 0.97 | 0.98 |

**Fv is the volume factor calculated for each alteration zone based on composition-volume diagrams

## Discussion

### Paragenetic sequence

Based on mineral-mutual relations, the paragenetic sequence of the ore and alteration minerals within the Dara copper mine area is summarized in Fig. 12. Magnetite, pyrrhotite, and probably chalcopyrite are of primary magmatic origin and have been observed among the constituents of the country rocks (gabbro-diorite, diorite, and granodiorite). Under hydrothermal conditions, secondary sericite (after feldspars) and pyrite (after pyrrhotite and magnetite) were formed in the proximal sericite zone. Subsequently, the formation of chlorite and secondary magnetite/hematite at the response of the breakdown of ferromagnesian minerals (e.g., hornblende) has occurred in the distal chlorite zone. Martitized magnetite recorded in the sericite alteration zone may reflect enhancing oxidized conditions during the alteration process. Little silicification signs contemporaneous with sericitization were recorded. Eventually, quartz veins have been precipitated enclosing clusters of sulfides (common pyrite and scarce chalcopyrite) and sericite. Later, supergene alteration of copper

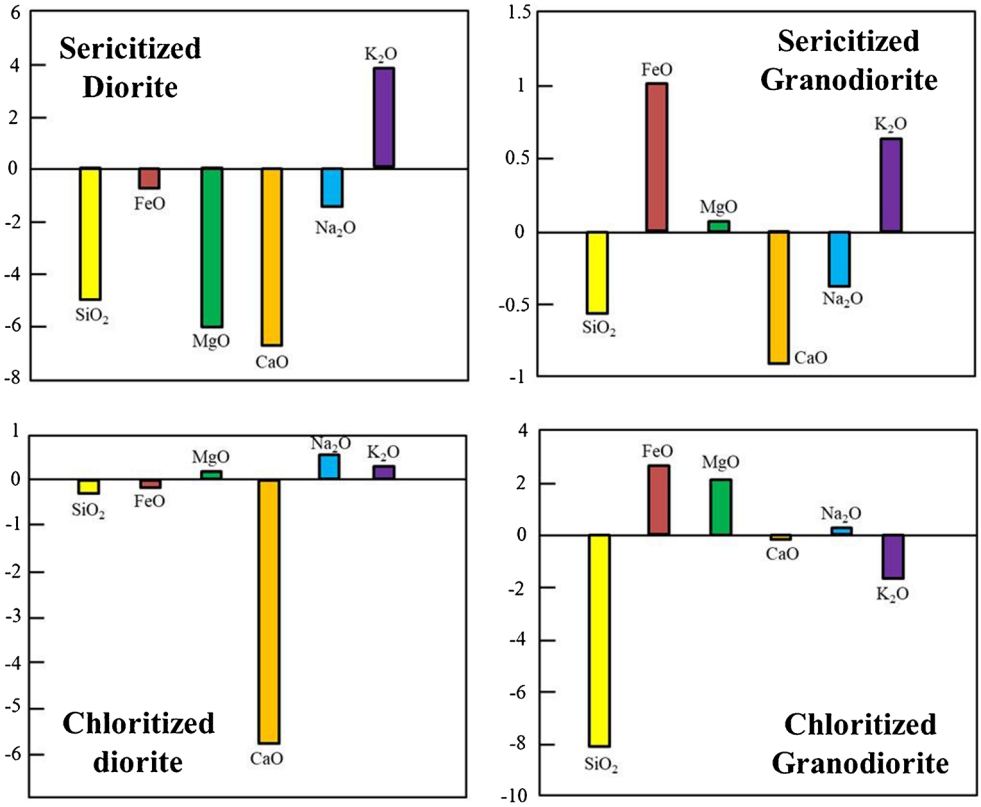


**Fig. 10** Gain-loss diagram for major oxides in the sericite and chlorite alteration zones encountered in the diorite and granodiorite host rocks in the Dara copper mine area

and iron minerals (e.g., chalcopyrite, pyrite, magnetite), most probably due to circulating meteoric water, led to the formation of covellite, malachite, and goethite.

## Alteration processes

The alteration processes in the Dara copper mine area are reflected in the elemental remobilization and ore mineral formation. Based on the petrographic textural relationships, these processes along with ore mineralization can be chronologically arranged from sericitization through sulfidization to chloritization and eventually silicification.

Initial high $K^+$ and $H^+$ activities for the invading fluids are suggested by the sericitization process. Sericitization of plagioclase in the sericite zone that developed in both diorite and granodiorite can be reproduced by the following reaction:

$$3\,[(Na, Ca)AlSi_3O_8] + K^+ + 2H^+ \;==\; [KAl_3Si_3O_{10}(OH)_2] + 6SiO_2 + 3(Na^+, Ca^{2+}) \quad (1)$$

plagioclase fluid sericite quartz fluid

The reaction reveals the release of Na, Ca, and Si ions, which is consistent with the microscopic observation of sericitized plagioclase and mass balance equations mentioned above. However, the formation of sericite in the chlorite zone that developed in granodiorite cannot be explained by the above reaction, where removal rather than the addition of $K_2O$ was recognized from the mass balance calculations (Eq. 4). This may be explained either by sericitization due to destabilization of K-feldspar according to the reaction

$$3KAlSi_3O_8 + 2H^+ == KAl_3Si_3O_{10}(OH)_2 + 6SiO_2 + 2K^+ \quad (2)$$

orthoclase fluid sericite quartz fluid

or by the action of two stages of hydrothermal fluids, where the first stage is characterized by higher $K^+$ activity. However, the liberation of K along with Fe and Mg due to the breakdown of ferromagnesian minerals, like biotite, during hydrothermal alteration was also documented (e.g., Ferry 1979; Fiebig and Hoefs 2002). This is consistent with the mass balance calculations of the diorite host (see Eq. 1). However, adding rather than leaching of FeO and MgO can be recognized in the sericitized granodiorite variety, the feature which may be plausibly explained by two successive hydrothermal stages, where the fluids of the second stage became enriched in iron and magnesium.

The increase of $Fe^{2+}/Fe^{3+}$ ratio could increase the concentration of reducing agents such as $H_2$ and $H_2S$ in the fluids (Kerrich et al. 1977; Pirajno and Smithies 1992; Huston 2001; Williams-Jones and Heinrich 2005). The observed sulfides (e.g., chalcopyrite, pyrite) and mass balance calculations of trace elements in the sericite zone developed in the diorite host seem to reflect such relation. In the second hydrothermal stage, however, adding FeO could precipitate iron oxides as magnetite ± hematite in the sericitized

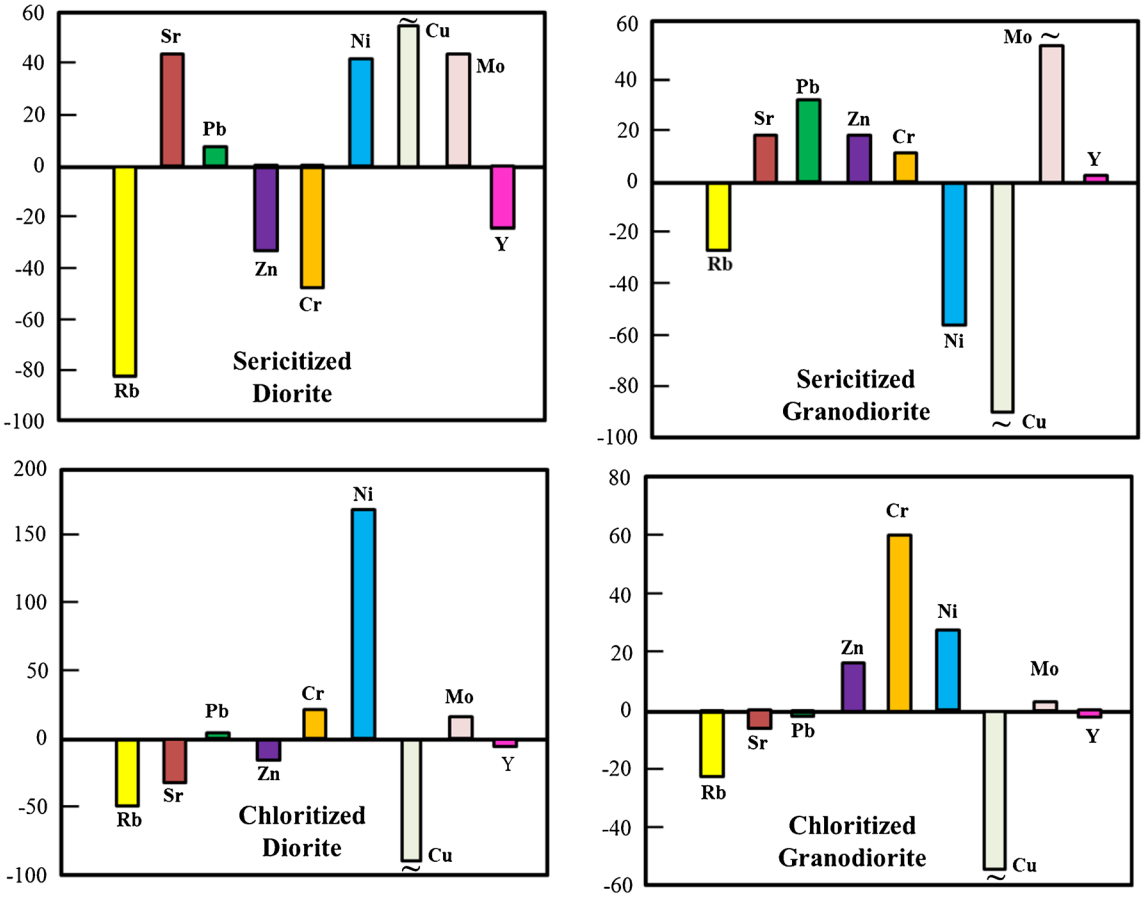


**Fig. 11** Gain-loss diagram for selected trace elements in the sericite and chlorite alteration zones recognized in the diorite and granodiorite host rocks in the Dara copper mine area

**Fig. 12** Paragenetic sequence for ore and alteration minerals in the Dara copper mine area. Colored-line thickness indicates approximate relative mineral abundance

| | Magmatic stage | Hydrothermal stages | | | | Supergene stage |
|---|---|---|---|---|---|---|
| | | Sericitization | sulfidization | chloritization | silicification | |
| Magnetite | | | | | | |
| Pyrrhotite | | | | | | |
| Chalcopyrite | | | | | | |
| Sericite | | | | | | |
| Pyrite | | | | | | |
| Chlorite | | | | | | |
| Hematite | | | | | | |
| Quartz | | | | | | |
| Covellite | | | | | | |
| Malachite | | | | | | |
| Goethite | | | | | | |

granodiorite under oxidizing rather than reducing conditions, which favorite leaching copper in this stage. Moreover, leaching of Zn and Cr, due to breakdown of ferromagnesian minerals, in the sericitized diorite despite adding them in the sericitized granodiorite can be considered as another good evidence of two successive stages of hydrothermal activities.

The sericitization process could affect the pH of the invading fluids and consequently the degree of dissociation of hydrogen-containing complexes, which in turn affects the solubility of metals in the hydrothermal fluids (Guilbert and Park 1986; Pirajno 2010). Consuming $H^+$ through the sericitization process could raise the pH of the invading fluids to become more alkaline (Robb 2005; Pirajno 2010). The ore minerals observed in the sericite zone that developed in the diorite host (with abundant pyrite and minor chalcopyrite) indicate decreasing $aH^+$ and oxygen fugacity in the hydrothermal fluids, conditions favorite for leaching copper rather than precipitating it as copper sulfides (Seward and Barnes 1997; Seward et al. 2014). According to this scenario, the recognized magnetite in the sericite zone is most probably of magmatic origin. The development of micro ilmenite exsolution in magnetite from the sericitized diorite may support this interpretation (Nadoll et al. 2015). In the sense of mass balance calculations, Na liberated from plagioclase destruction (Eqs. 1 and 2) during the sericitization process could be responsible for increasing the alkalinity of the fluids. Under such conditions, copper is more likely transported in the form of Cl complexes (Mountain and Seward 1999, 2003). On the other hand, adding Cu, Mo, and Ni in the sericite zone of the diorite host (Table 4, Fig. 11) may indicate their high contents in the invading hydrothermal fluids.

Unexpectedly, Pb and Sr (partitioned mainly in feldspars) are gained rather than lost in the sericite-pyrite alteration zone (Table 4, Fig. 11). The most plausible explanation for this may be the partitioning of Pb in sericite on one hand and partitioning of Sr in apatite (Ca-bearing mineral) on the other. Both minerals are abundant in the sericite-pyrite zone and have been suggested as capturing phases for Pb and Sr in other alteration systems, respectively (Li et al. 2013; Hikov 2013; Georgieva and Hikov 2016). Zinc, most probably liberated from the breakdown of ferromagnesian minerals, is subtracted from altered diorite (richer in ferromagnesian minerals) and added to altered granodiorite. Here it should be noted that Zn is more mobile than Pb under hydrothermal conditions (Large et al. 2001).

Chloritization has followed the sericitization and sulfidization processes in the Dara copper mine area. After sericitization, the hydrothermal fluids became richer in $Mg^{2+}$ and $Fe^{2+}$ most probably due to the decomposition of ferromagnesian minerals in the sericitized zone. Moreover, the formation of sericite and sulfides in the sericitized zone can be considered as an effective factor in decreasing $K^+$ and $Fe^{2+}$ ions in the invading fluids and hence resulting in minimum precipitation of sulfides in the chlorite zone. The enhanced Mg and, to less extent, $Fe^{2+}/Fe^{3+}$ activities in the chlorite-sericite zone can lead to the formation of hydrothermal chlorite (e.g., Helba et al. 2001; Wu et al. 2019) according to the equation:

$$[KAlSi_3O_8] + 6.5Mg^{2+} + 10H_2O = \left[Mg_{6.5}(Si_3Al)O_{10}(OH)_8\right] + K^+ + 12H^+$$

K-feldspar fluid chlorite fluid

This equation could also explain the formation of sericite in the chlorite-sericite zone, where $K^+$ and $H^+$ produced from the chloritization process could cause hydrolysis for pre-existing plagioclase to form considerable amounts of sericite in this zone.

Precipitation of the quartz veins may represent the last stage of the hypogene hydrothermal activity in the study area. This assumption is evidenced by the paragenetic sequence based on the textural relations of the investigated minerals, as mentioned above, and also supported by the mass balance calculations, where leaching of silica from the different alteration zones was documented (Fig. 10). Subsequent supergene alterations under surficial oxidizing conditions have affected the rocks in the study area due to reactions with $CO_2$-bearing circulating meteoric water, which led to the formation of minerals such as goethite, malachite, and covellite. Goethite, more abundant in the chlorite alteration zone, represents the uppermost phase of the supergene minerals. Malachite was observed as green staining along fracture planes. It appears (along with covellite) as scattered grains in the alteration zones, more abundant in the sericite one (Fig. 6e).

Hydrothermal fluids and the type of mineralization

Hydrothermal fluids responsible for transporting and precipitating ore deposits in the basement rocks of the Eastern Desert of Egypt are related either to magmatic activity (relevant to older granite intrusions) or metamorphic events associating the convergent tectonic stages that led to the formation of greenschist metamorphic terrains in the Neoproterozoic crust of Egypt (Khalil et al. 2016; Zoheir et al. 2019 and references therein). The metamorphic-related hydrothermal fluids are characterized generally by high $CO_2$ and low salinity and are commonly associated with carbonate alteration zones (e.g., Harraz 2002; Helmy and Zoheir 2015). No mineralogical or alteration evidence on such characteristics could be detected in the study area; neither carbonate-bearing veins nor distinct carbonate alteration zones were observed. Evidence from fluid inclusions and stable isotope data has supported a magmatic origin of these fluids (Al-Boghdady et al. 2003). Confirming evidence of such origin is presented in the following paragraphs.

The dioritic rocks, which host the mineralized quartz veins in the Dara area, possess I-type granite characters (i.e., A/

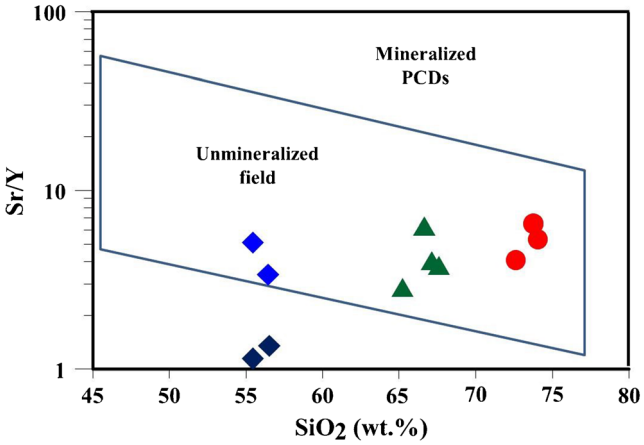


**Fig. 13** The plot of the Dara granitoid rocks in the Sr/Y versus $SiO_2$ discriminant diagram of Rohrlach and Loucks (2005)

CNK< 1.1 and $Na_2O$ > 2.2, Chappell and White 1974 and 2001) (Fig. 8d) and belong to the magnetite series granites of Ishihara (1977, 1981), where magnetite is the dominant opaque mineral in these rocks. These features indicate oxidizing conditions prevailing during their crystallization and may suggest that the hydrothermal fluids, of the same characters as deduced from their alteration products as described above, belong to these magmatic events. These features may resemble that of intermediate rocks associated with porphyry copper mineralization formed under oxidizing conditions at subduction zones of Andean type (Sillitoe 1972; Richards 2003; Sillitoe 2010 and references therein). Repeated cycles of replenishment for intermediate melts via fractional crystallization of hornblende have been suggested as the main mechanism for upgrading Cu concentration in such porphyry copper deposits (Sillitoe 1998; Garwin et al. 2005; Rohrlach and Loucks 2005; Cloos and Housh 2008; Cooke et al. 2011). Upgrading Cu through these cycles was attributed to the incompatibility of copper in the magmatic melt, where it partitions likely in residual fluids before its separation and/or precipitation through hydrothermal activity.

In such cases, porphyry copper-related intermediate rocks will maintain a high Sr/Y ratio, where fractional crystallization of hornblende, the main host of Y, leads to increasing Sr/Y ratio in magmatic melts (Williams-Jones and Heinrich 2005; Sillitoe 2010; Weis et al. 2012; Heinrich and Candela 2014). The examined diorite and porphyritic granodiorite, however, have low Sr/Y ratios at a given $SiO_2$ content (Fig. 13), the character that cannot be explained by the formation of the copper mineralization in the Dara area as a part of a porphyry copper system. Instead, the ore mineral association (abundant magnetite and pyrite) and alteration geochemistry suggest that the Dara copper mineralization is pertaining most probably to the iron oxide-copper-gold (IOCG) deposits. However, more evidences are needed to support our preliminary conclusion about the origin of this Cu mineralization type.

## Conclusions

The copper mineralization of the Dara area is structurally controlled and is hosted mainly in sheared diorite and granodiorite. The host rocks show petrological and geochemical characteristics of calc-alkaline I-type affinity. The diorite has metaluminous nature and was formed by mantle-derived fractionated magma. The granodiorite, on the other hand, has mild-metaluminous nature and was formed in a pre-collision setting.

The mineralogical, geochemical, and mass balance study of the alteration patterns associating copper mineralization in the Dara area revealed the following conclusions:

– Sericitization, sulfidization, chloritization, and silicification are the main successive alteration processes that accompanied the hydrothermal activities in the Dara copper mine area.

– Two stages of hydrothermal solutions can be inferred based on the mineralogical features and mass balance calculations. The first stage is more effective and was responsible for precipitating copper in the study area.

– Magmatic rather than metamorphic origin for the hydrothermal fluids is suggested, and the physicochemical conditions of their formation indicate that the recognized hydrothermal fluids may be genetically related to the emplacement of the granodiorite host rock.

– The gabbro-diorite host could be an important source of copper and related elements in the study area.

– Most probably, the Dara copper mineralization belongs to the magmatic-hydrothermal iron oxide-copper-gold (IOCG) deposit category formed under oxidizing conditions rather than to the porphyry copper system. Detailed genetic study for ore minerals is recommended for confirming this conclusion.

**Supplementary Information** The online version contains supplementary material available at https://doi.org/10.1007/s12517-021-07495-4.

**Acknowledgements** The authors are grateful to the Egyptian Mineral Resources Authority (EMRA) for the immense support of this study and assistance with sample processing and analysis. The fruitful discussion with Prof. K.I. Khalil is greatly appreciated. The authors would like to thank Mr. M. Moheb for technical assistance with thin and polished sections preparation. The authors also thank the reviewers Prof. S. Al-Khirbash and Prof. I.A. Abboud for their constructive and valuable comments and advising.

## Declarations

**Conflict of interest** The authors declare that they have no competing interests.

## References

Abdel Magid EA, Khyamy AA, Mostafa MO, Mohamed HA, Abdel Gawad GM, Ibrahim GA (1998) Geology of Gabal Monqul and

Gabal Dara area, north Eastern Desert, Egypt. Egyptian Mineral Resource Authority (EMRA), Internal Report 91

Abdel Rahman AM, Doig R (1987) The Rb-Sr geochronological evolution of the Ras Gharib segment of the northern Nubian Shield. J Geol Soc Lond 144:577–586

Ahmed HA, Gharib ME (2016) Porphyry Cu mineralization in the eastern desert of Egypt: inference from geochemistry, alteration zones, and ore mineralogy. Arab J Geosci 9(179):1–26

Al-Boghdady AA, Bishady AM, Shalaby MH, Bassiouni MI (2003) Copper mineralization of Wadi Dara area, north Eastern Desert, Egypt: fluid inclusions and mineral chemistry evidence. 5th International Conference on the Geology of the Middle East, 643-658

Ali KA, Kröner A, Hegner E, Wong J, Li SQ, Gahlan HA, ElEla FF (2015) U-Pb zircon geochronology and Hf-Nd isotopic systematics of Wadi Beitan granitoid gneisses, south Eastern Desert, Egypt. Gondwana Res 27:811–824

Babcock RS (1973) Computational models of metasomatic processes. Lithos 6:279–290

Barton MD, Johnson DA (2000) Alternative brine sources for Fe-oxide (Cu-Au) systems: implications for hydrothermal alteration and metals, in Porter, T.M., ed., Hydrothermal Iron Oxide Copper-Gold and Related Deposits: A Global Perspective, Volume 1: Adelaide, Australian Mineral Foundation 43–60.

Batchelor RA, Bowden P (1985) Petrogenetic interpretation of granitoid rock series: using multinational parameters. Chem Geol 48:43–55

Bishady AM, Shalaby MH, Eliwa HA, Bassuoni MI (2001) Mineralogical and geochemical studies on the copper mineralized rocks of Wadi Dara area, north Eastern Desert. Egypt Al-Azhar Bull Sci 4:393–430

Botros NS, Wetait MA (1997) Possible porphyry copper mineralization in south Um Monqul, Eastern Desert, Egypt. Egypt J Geol 41(1): 175–196

Chappell BW, White AJR (1974) Two contrasting granite types. Pac Geol 8:173–174

Chappell BW, White AJR (1992) I- and S-type granites in the Lachlan Fold Belt. Trans R Soc Edinb Earth Sci 83:1–26

Chappell BW, White AJR (2001) Two contrasting granite types – 25 years later. Aust J Earth Sci 48:489–499

Cloos M, Housh TB (2008) Collisional delamination—implications for porphyry-type Cu-Au ore formation in New Guinea. In: Spencer JE, Titley SR (eds). Ores and orogenesis: Circum-Pacific tectonics, geologic evolution, and ore deposits: Arizona Geological Society Digest 22:235–244

Cooke DR, Hollings P, Chang Z (2011) Philippine porphyry and epithermal deposits. Econ Geol 106:1253–1256

Cooke DR, Hollings P, Wilkinson JJ, Tosdal RM (2014) Geochemistry of porphyry deposits. In: Turekian HD, Holland KK (eds) Treatise on Geochemistry, 2nd edn. Elsevier, Oxford, pp 357–381

El-Desoky HM, Hafez HM (2018) Petrology and mineralogy of the hydrothermally altered rock units at Wadi Dara, north Eastern Desert, Egypt. Ann Geol Surv Egypt 35:103–140

Ferry JM (1979) Reaction mechanisms, physical conditions, and mass transfer during hydrothermal alteration of mica and feldspar in granitic rocks from south-central Maine, USA. Contrib Mineral Petrol 68:125–139

Fiebig J, Hoefs J (2002) Hydrothermal alteration of biotite and plagioclase as inferred from intragranular oxygen isotope- and cation-distribution patterns. Eur J Mineral 14:49–60

Fritz H, Abdelsalam M, Ali KA, Bingen B, Collins AS, Fowler AR, Ghebreab W, Hauzenberger CA, Johnson PR, Kusky TM, Macey P, Muhongo S, Stern RJ, Viola G (2013) Orogen styles in the East African Orogen: a review of the Neoproterozoic to Cambrian tectonic evolution. J Afr Earth Sci 86:65–106

Garwin S, Hall R, Watanabe Y (2005) Tectonic setting, geology, and gold and copper mineralization in Cenozoic magmatic arcs of Southeast Asia and the West Pacific: Society of Economic Geologists, Economic Geology 100th Anniversary 891–930

Georgieva S, Hikov A (2016) Geochemistry of hydrothermally altered rocks from the Chelopech high-sulphidation Cu-Au deposit, Bulgaria. C R Acad Bulg Sci 69(6):761–768

Gifkins CC, Herrmann W, Large RR (2006) Altered volcanic rocks: a guide to description and interpretation. Centre for Ore Deposit Research, University of Tasmania: Hobart, Australia 275.

Grant JA (1986) The isocon diagram-a simple solution to Gresens' equation for metasomatic alteration. Econ Geol 81:1976–1982

Greiling RO, Abdeen MM, Dardir AA, El Akhal H, El Ramly MF, Kamal El Din GM, Osman AF, Rashwan AA, Rice AHN, Sadek MF (1994) A structural synthesis of the Proterozoic Arabian-Nubian Shield in Egypt. Geol Rundsch 83:484–501

Gresens RL (1967) Composition - volume relations of metasomatism. Chem Geol 2:47–65

Groves DI, Bierlein FP, Meinert LD, Hitzman MW (2010) Iron oxide copper-gold (IOCG) deposits through Earth history: implications for origin, lithospheric setting, and distinction from other epigenetic iron oxide deposits. Econ Geol Bull Soc Econ Geol 105:641–654

Guilbert JM, Park CF (1986) The geology of ore deposits. WH Freeman and Co., New York 985

Harraz HZ (2002) Fluid inclusions in the mesozonal gold deposit at Atud mine, Eastern Desert, Egypt. J Afr Earth Sci 35:347–363

Hedenquist JW, Taguchi S, Shinohara H (2018) Features of large magmatic–hydrothermal systems in Japan: characteristics similar to the tops of porphyry copper deposits. Resour Geol 68(2):164–180

Heinrich CA, Candela PA (2014) Fluids and ore formation in the earth's crust treatise on geochemistry (2nd edition) Elsevier 1–28.

Helba HA, Khalil KI, NMF A (2001) Alteration patterns related to hydrothermal gold mineralization in meta-andesites at Dungash area, Eastern Desert, Egypt. Resour Geol 51(1):19–30

Helmy HM, Zoheir BA (2015) Metal and fluid sources in a potential world-class gold deposit: El-Sid mine, Egypt. Int J Earth Sci 104: 645–661

Hikov A (2013) Geochemistry of hydrothermally altered rocks from the Asarel porphyry copper deposit, Central Srednogorie. Geologica Balcanica 42:3–28

Hitzman MW, Oreskes N, Einaudi MT (1992) Geological characteristics and tectonic setting of Proterozoic iron oxide (Cu-U-Au-REE) deposits. Precambrian Res 58:241–287

Hussein AA (1990) Mineral deposits chapter. In: Said R (ed), The geology of Egypt. Balkema, Rotterdam 511–566

Hussein AA, Shalaby IM, Gad MA, Rasmy AH (1977) On the origin of Zn-Cu-Pb deposits at Um Samiuki, Eastern Desert, Egypt. 15th Annual Meeting. Geol Soc Egypt (Abstract)

Huston DL (2001) Geochemical dispersion about the Western Tharsis Cu-Au deposit, Mt Lyell, Tasmania. J Geochem Explor 72:23–46

Irvine TN, Baragar WRA (1971) A guide to the chemical classification of the common volcanic rocks. Can J Earth Sci 8:523–548

Ishihara S (1977) The magnetite-series and ilmenite-series granitic rocks. Mining Geology 26:293–305

Ishihara S (1981) The granitoid series and mineralization. Economic Geology, 75th Anniversary 458–584

Ishikawa Y, Sawaguchi T, Iwaya S, Horiuchi M (1976) Delineation of prospecting targets for Kuroko deposits based on modes of volcanism of underlying dacite and alteration halos. Min Geol 26:105–117

Ivanov TG, Hussein AA (1972) Assessment of the mineral potential of the Aswan region. Technical report on the geological operations carried out from July 1968 to. Egyptian Geological Survey, Internal Report, No:68/73

Johnson PR, Andresen A, Collins AS, Fowler AR, Fritz H, Ghebreab W, Kusky T, Stern RJ (2011) Late Cryogenian-Ediacaran history of the Arabian-Nubian Shield: a review of depositional, plutonic,

structural, and tectonic events in the closing stages of the northern East African Orogen. J Afr Earth Sci 10:1–179

Kerrich R, Fyfe WS, Allison I (1977) Iron reduction around gold-quartz veins, Yellowknife District, Northwest Territories, Canada. Econ Geol 72:657–663

Khalifa IH, Hegazi AM, Faisal M (2016) The geological setting for porphyry copper deposits in calc-alkaline rocks: Wadi Rofaiyed area, Sinai, Egypt. Arab J Geosci 9:1–22

Khalil IK, Moghazi AM, El Makky AM (2016) Nature and geodynamic setting of late Neoproterozoic vein-type gold mineralization in the Eastern Desert of Egypt: mineralogical and geochemical constraints. In: Bouabdellah M, Slack JF (eds), Mineral deposits of North Africa, Berlin-Heidelberg, Springer-Verlag, 353-370

Large RR, Gemmell JB, Paulick H, Huston DL (2001) The alteration box plot: a simple approach to understanding the relationship between alteration mineralogy and lithogeochemistry associated with volcanic-hosted massive sulfide deposits. Econ Geol 96:957–971

Le Maitre RW, Streckeisen A, Zanettin B, Le Bas MJ, Bonin B, Bateman P (2002) Igneous rocks: a classification and glossary of terms (2nd edition) Cambridge University Press 236.

Leitch CHB, Lentz DR (1994) The Gresens approach to mass balance constraints of the alteration systems: methods, pitfalls, examples. In Alteration and Alteration Processes Associated with Ore-Forming Systems; Lentz DR (ed), Geological Association of Canada: St. John's, NL, Canada 11 161–192

Li XC, Fan HR, Santosh M, Hu FF, Yang KF, Lan TG (2013) Hydrothermal alteration associated with Mesozoic granite-hosted gold mineralization at the Sanshandao deposit, Jiaodong Gold Province, China. Ore Geol Rev 53:403–421

Maniar PD, Piccoli PM (1989) Tectonic discrimination of granitoids. Geol Soc Am Bull 101:636–643

Mathieu L (2018) Quantifying hydrothermal alteration: a review of methods. Geosciences 8(245):1–27

Miyashiro A (1974) Volcanic rock series in island arcs and active continental margins. Am J Earth Sci 274:321–355

Mountain BW, Seward TM (1999) The hydrosulphide/sulphide complexes of copper (I): experimental determination of the stoichiometry and stability at 22° C and reassessment of high-temperature data. Geochim Cosmochim Acta 63:11–29

Mountain BW, Seward TM (2003) Hydrosulphide/sulphide complexes of copper (I): experimental confirmation of the stoichiometry and stability of $Cu(HS)_2$ - to elevated temperatures. Geochim Cosmochim Acta 67:3005–3014

Mumin AH, Somarin AK, Jones B, Corriveau L, Ootes L, Camier J (2010) The IOCG porphyry-epithermal continuum of deposit types in the Great Bear magmatic zone, Northwest Territories, Canada. In: Corriveau, L, Mumin H (eds). Exploring for Iron Oxide Copper-Gold Deposits: Geological Association of Canada Short Course Notes 20:59–78

Nadoll P, Mauk JL, Leveille RA, Koenig AE (2015) Geochemistry of magnetite from porphyry Cu and skarn deposits in the southwestern United States. Mineral Deposita 50:493–515

Neal LC, Wilkinson JJ, Mason PJ, Chang Z (2018) Spectral characteristics of propylitic alteration minerals as a vectoring tool for porphyry copper deposits. J Geochem Explor 184:179–198

Peccerillo A, Taylor SR (1976) Geochemistry of Eocene calc-alkaline volcanic rocks from the Kastamonu area, northern Turkey. Contrib Mineral Petrol 58:63–81

Pirajno F (2010) Hydrothermal processes and mineral systems. Springer Science and Business Media, 1250

Pirajno F, Smithies RH (1992) The FeO/Feo + MgO ratio of tourmaline: a useful indicator of spatial variations in granite-related hydrothermal mineral deposits. J Geochem Explor 42:371–382

Rasmy AH (1982) Mineralogy of copper-nickel mineralization at Akarem area. Ann Geol Surv Egypt 12:141–162

Richards JP (2003) Tectono-magmatic precursors for porphyry Cu-(Mo-Au) deposit formation. Bull Soc Econ Geol 98:1515–1533

Richards JP, Mumin AH (2013) Magmatic-hydrothermal processes within an evolving Earth: iron oxide-copper-gold and porphyry Cu ± Mo ± Au deposits. Geology 41(7):767–770

Robb L (2005) Introduction to ore-forming processes. Blackwell Science Ltd., 386 p

Rohrlach BD, Loucks RR (2005) A multi-million-year cyclic ramp-up of volatiles in a lower crustal magma reservoir trapped below the Tampakan copper-gold deposit by Mio-Pliocene crustal compression in the southern Philippines, in TM Porter (ed), super porphyry copper and gold deposits: a global perspective: PGC Publishing, 2 270

Seward TM, Barnes HL (1997) Metal transport in hydrothermal ore fluids. In: Barnes HL (ed) Geochemistry of Hydrothermal Ore Deposits, 3rd Edition 435–486. New York: Wiley Interscience

Seward TM, Williams-Jones AE, Migdisov AA (2014) The chemistry of metal transport and deposition by ore-forming hydrothermal fluids. In: Holland HD and Turekian KK (eds), Treatise on geochemistry, 2nd Edition 13 29-57. Oxford Elsevier

Sillitoe RH (1972) A plate tectonic model for the origin of porphyry copper deposits. Econ Geol 67:184–197

Sillitoe RH (1998) Epochs of intrusion-related copper mineralization in the Andes: Journal of South American Earth Sciences 1:89–108

Sillitoe RH (2010) Porphyry copper systems. Econ Geol 105:3–41

Stern RJ (2018) Neoproterozoic formation and evolution of Eastern Desert continental crust–the importance of the infrastructure-superstructure transition. J Afr Earth Sci 146:15–27

Stern RJ, Hedge CE (1985) Geochronologic and isotopic constraints on Late Precambrian crustal evolution in the Eastern Desert of Egypt. Am J Sci 285:97–127

Wedepohl KH (1995) The composition of the continental crust. Geochim Cosmochim Acta 59(7):1217–1232

Weis P, Dresner T, Heinrich CA (2012) Porphyry-copper ore shells form at stable pressure-temperature fronts within dynamic fluid plumes. Science 338:1613–1616

Wilkinson JJ, Chang Z, Cooke DR, Baker MJ, Wilkinson CC, Inglis S, Chen H, Gemmell JB (2015) The chlorite proximitor: a new tool for detecting porphyry ore deposits. J Geochem Explor 152:10–26

Williams PJ, Barton MD, Fontboté L, de Haller A, Johnson DA, Mark G, Marschik R, Oliver NHS (2005) Iron-oxide-copper-gold deposits: geology, space-time distribution, and possible modes of origin: Economic Geology 100th Anniversary 371–406.

Williams-Jones AE, Heinrich C (2005) Vapor transport of metals and the formation of magmatic-hydrothermal ore deposits. Econ Geol 100: 1287–1312

Wu D, Pan J, Xia F, Huang G, Lai J (2019) The mineral chemistry of chlorites and its relationship with uranium mineralization from Huangsha uranium mining area in the middle Nanling Range, SE China. Minerals 9(199):1–23

Zaki ME (1996) Preliminary report on the results of geochemical prospecting in the areas of Um Balad, Dara, Mongul and Wadi Dib, north Eastern Desert. Geological Survey of Egypt Unpublished report No 43/96.

Zoheir BA, Johnson PR, Goldfarb RJ, Klemm DD (2019) Orogenic gold in the Egyptian Eastern Desert: widespread gold mineralization in the late stages of Neoproterozoic orogeny. Gondwana Res 75:184–217